Nuclear SUN1 Stabilizes Endothelial Cell Junctions via Microtubules to Regulate Blood Vessel Formation

Danielle B Buglak[a], Molly R Kulikauskas[a], Ziqing Liu[b], Ariel L Gold[b], Allison P Marvin[b], Andrew Burciu[b], Natalie T Tanke[a], Shea N Ricketts[c], Karina Kinghorn[a], Morgan Oatley[b], Bryan N Johnson[b], Pauline Bougaran[b], Celia E Shiau[b], Stephen L Rogers[b], and Victoria L Bautch[a,b,d,#]

[a]Curriculum in Cell Biology and Physiology, The University of North Carolina at Chapel Hill, Chapel Hill, North Carolina 27599, USA.
[b]Department of Biology, The University of North Carolina at Chapel Hill, Chapel Hill, North Carolina 27599, USA.
[c]Department of Pathology, The University of North Carolina at Chapel Hill, Chapel Hill, North Carolina 27599, USA.
[d]McAllister Heart Institute, The University of North Carolina at Chapel Hill, Chapel Hill, North Carolina 27599, USA

[#]Corresponding author: Victoria L Bautch, PhD
Professor of Biology
Department of Biology, CB#3280
University of North Carolina at Chapel Hill
Chapel Hill, NC 27599 USA
E-mail: bautch@med.unc.edu

Running head: SUN1 Regulates Endothelial Junctions and Angiogenesis

Abstract: 206 words
Text: 47,835 characters with spaces (including figure legends; excluding methods, references, and supplement)
Figures: 7 main, 8 supplemental, 6 movies
References: 113

50 **SUMMARY**

51 The nuclear membrane protein SUN1 promotes blood vessel formation and barrier
52 function by stabilizing endothelial cell-cell junctions. Communication between SUN1 and
53 endothelial cell junctions relies upon proper microtubule dynamics and Rho signaling far
54 from the nucleus, revealing long-range cellular communication from the nucleus to the
55 cell periphery that is important for vascular development and function.

56

ABSTRACT

Endothelial cells line all blood vessels, where they coordinate blood vessel formation and the blood-tissue barrier via regulation of cell-cell junctions. The nucleus also regulates endothelial cell behaviors, but it is unclear how the nucleus contributes to endothelial cell activities at the cell periphery. Here we show that the nuclear-localized LINC complex protein SUN1 regulates vascular sprouting and barrier function via effects on endothelial cell-cell junction morphology and function. Loss of murine endothelial *Sun1* impaired blood vessel formation and destabilized junctions, angiogenic sprouts formed but retracted in SUN1-depleted sprouts, and zebrafish vessels lacking Sun1b had aberrant junctions and defective cell-cell connections. At the cellular level, SUN1 stabilized endothelial cell-cell junctions, promoted barrier function, and regulated contractility. Mechanistically, SUN1 depletion altered cell behaviors via the cytoskeleton without changing transcriptional profiles. Reduced peripheral microtubule density, fewer junction contacts and increased catastrophes accompanied SUN1 loss, and microtubule depolymerization phenocopied effects on junctions. Depletion of GEF-H1, a microtubule-regulated Rho activator, or the LINC complex protein nesprin-1 rescued defective junctions of SUN1-depleted endothelial cells. Thus, endothelial SUN1 regulates peripheral cell-cell junctions from the nucleus via LINC complex-based microtubule interactions that affect peripheral microtubule dynamics and Rho-regulated contractility, and this long-range regulation is important for proper blood vessel sprouting and barrier function.

Keywords: Endothelial cell, SUN1, LINC, nucleus, junctions, angiogenesis, microtubules, contractility, Rho, GEF-H1, nesprin-1

82 **INTRODUCTION**

83 Blood vessels form and expand via sprouting angiogenesis, a dynamic process
84 whereby endothelial cells migrate from pre-existing vessels to form new conduits
85 (Carmeliet & Jain, 2011; Wacker & Gerhardt, 2011; Kushner & Bautch, 2013; Bautch &
86 Caron, 2015). During angiogenesis, endothelial cell-cell junctions destabilize and
87 rearrange to allow for repolarization and migration towards pro-angiogenic cues (Esser
88 et al., 1998; Dejana, 2004; Blum et al., 2008). Specifically, the endothelial cell adherens
89 junction protein VE-cadherin is required for vascular sprouting and viability (Carmeliet et
90 al., 1999; Montero-Balaguer et al., 2009; Sauteur et al., 2014; Szymborska & Gerhardt,
91 2018). As vessels mature, endothelial cell junctions stabilize and form a functional
92 barrier that regulates egress of fluid and oxygen; barrier dysfunction leads to increased
93 permeability and severe disease (Claesson-Welsh, 2015; Rho et al., 2017; Claesson-
94 Welsh et al., 2021). Thus, regulation of endothelial cell junction stability is important
95 developmentally and for vascular homeostasis.
96

97 Adherens junctions are key to integrating and regulating both external and
98 internal cellular inputs from multiple sources, including the microtubule and actin
99 cytoskeletons (Ligon et al., 2001; Shaw et al., 2007; Bellett et al., 2009; Dejana &
100 Vestweber, 2013; Abu Taha & Schnittler, 2014). For example, increased actomyosin
101 contractility destabilizes endothelial cell adherens junctions, and disorganized junctional
102 actin accompanies VE-cadherin loss (Huveneers et al., 2012; Sauteur et al., 2014;
103 Angulo-Urarte et al., 2018). VE-cadherin loss also changes microtubule dynamics, and
104 disruption of microtubule dynamics destabilizes junctions and barrier function
105 (Komarova et al., 2012). Coordination of inputs from the actin and microtubule
106 cytoskeletons regulates endothelial cell barrier integrity and sprouting dynamics via

107 small GTPases (Birukova et al., 2006; Mavria et al., 2006; Sehrawat et al., 2008, 2011;
108 Wimmer et al., 2012; Szymborska & Gerhardt, 2018). In particular, RhoA signaling is
109 regulated by microtubules via GEF-H1, a RhoGEF that is inactive while bound to
110 microtubules and activated upon release, leading to RhoA activation, increased
111 actomyosin contractility, and changes to endothelial cell barrier function (Krendel et al.,
112 2002; Birukova et al., 2006; Birkenfeld et al., 2008). However, how the endothelial cell
113 nucleus affects these processes is poorly understood.
114
115 The nucleus is usually found far from the cell periphery and junctions, yet it is
116 important for functions critical to angiogenesis and vascular remodeling, such as
117 polarity, migration, and mechanotransduction (Tkachenko et al., 2013; Guilluy et al.,
118 2014; Graham et al., 2018), and perturbations of some nuclear membrane proteins
119 affect transcriptional profiles (Li et al., 2017; May & Carroll, 2018; Carley et al., 2021).
120 The linker of the nucleoskeleton and cytoskeleton (LINC) complex is comprised of both
121 SUN (Sad1p, UNC-84) and KASH (Klarsicht, ANC-1, Syne/Nesprin Homology) proteins
122 (Starr & Fridolfsson, 2010) that function as a bridge between the nucleus and the
123 cytoskeleton, and also link through subnuclear lamin filaments to chromatin (Haque et
124 al., 2006). SUN proteins localize to the inner nuclear membrane and bind KASH
125 proteins, or nesprins, from their C-terminus and lamins at their N-terminus, thus
126 providing a structural link from the nuclear cortex to the cellular cytoskeleton
127 (Padmakumar et al., 2005; Haque et al., 2006; McGee et al., 2006; Stewart-Hutchinson
128 et al., 2008). Nesprins are long spectrin-rich proteins localized to the outer nuclear
129 envelope that bind SUN proteins via their C-terminus while N-terminally interacting
130 indirectly with microtubules (via various motor proteins such as dynein and kinesin) and
131 intermediate filaments (via plectins), and directly with actin via calponin homology

132 domains (Ketema et al., 2007; Meyerzon et al., 2009; Zhang et al., 2009; Fridolfsson et
133 al., 2010; Starr & Fridolfsson, 2010). Two mammalian SUN proteins are ubiquitously
134 expressed, and based on functional consequences of SUN manipulations it has been
135 posited that SUN1 regulates microtubule-based functions while SUN2 coordinates actin
136 regulation (Zhu et al., 2017). However, *in vitro* binding studies do not reveal a SUN-
137 nesprin specificity to account for this bias (Stewart-Hutchinson et al., 2008; Ostlund et
138 al., 2009), so how complexes are assembled and sorted in cells is unclear. It is well-
139 established that the LINC complex integrates external inputs sensed by focal
140 adhesions, such as substrate stiffness, to regulate transcription (Carley et al., 2022), but
141 how the LINC complex relays signals from the nucleus to the cell periphery is less
142 understood.
143
144 The LINC complex functions in cultured endothelial cells, as knockdown of
145 nesprin-3 leads to impaired endothelial polarity under flow (Morgan et al., 2011), while
146 nesprin-2 and lamin A regulate proliferation and apoptosis in endothelial cells exposed
147 to shear stress (Han et al., 2015). Depletion of nesprin-1 alters tension on the nucleus
148 (Chancellor et al., 2010; Anno et al., 2012), and knockdown of nesprin-1 or nesprin-2
149 leads to reduced collective endothelial migration (Chancellor et al., 2010; King et al.,
150 2014). Recent work showed compromised matrix adhesion and barrier function of
151 cultured endothelial cells using a dominant negative KASH (Denis et al., 2021).
152 However, less is understood about the roles of the SUN proteins in endothelial cell
153 function.
154
155 The LINC complex is required for viability *in vivo*. Loss of both mammalian *Sun*
156 genes is embryonic lethal due to impaired neuronal nuclear migration required for

157 proper neuronal differentiation (Lei et al., 2009; Zhang et al., 2009). Global *Sun2* loss
158 affects epidermal nuclear positioning and cell adhesion, leading to alopecia (Stewart et
159 al., 2015), while global loss of both *Sun* genes impairs epidermal differentiation due to
160 altered integrin signaling (Carley et al., 2021). A role for the LINC complex in
161 mechanotransduction *in vivo* is suggested by findings that perturbations in mechanically
162 active skeletal and cardiac muscle affect function (Zhang et al., 2005, 2010; Lei et al.,
163 2009; Banerjee et al., 2014; Stroud et al., 2017; Zhou et al., 2017; van Ingen & Kirby,
164 2021). However, while global deletion of multiple LINC components to disrupt the entire
165 complex highlight its importance (Lei et al., 2009; Zhang et al., 2009; Carley et al.,
166 2021), these studies do not reveal functions of individual LINC components in specific
167 tissues. Whether the SUN proteins cell autonomously regulate the vascular
168 endothelium, which is also mechanically active due to outward pressure and shear
169 stress from blood flow, has not been explored.
170
171 Mutations in *LMNA* (lamin A/C) cause a premature aging syndrome linked to
172 cardiovascular defects (Capell & Collins, 2006). The LINC complex protein SUN1 is
173 mis-expressed in this disease (Chen et al., 2012), and cellular defects due to the *LMNA*
174 mutation are rescued by reduced levels of SUN1 protein, highlighting a potential
175 function for SUN1 in the disease pathology (Chen et al., 2012; Chang et al., 2019).
176 Here, we present an in-depth analysis of how the LINC complex component SUN1
177 affects blood vessel development and function *in vivo*. We found that *Sun1* cell-
178 autonomously regulates blood vessel sprouting and barrier function *in vivo,* and these
179 effects are consistent with SUN1 regulating endothelial cell functions via adherens
180 junction activity. In primary endothelial cells, nuclear SUN1 coordinates peripheral
181 microtubule dynamics that in turn regulate peripheral RhoGEF activation, junction

182 stability and barrier function. Thus, nuclear SUN1 that resides far from endothelial cell
183 junctions regulates endothelial cell-cell communication and blood vessel sprouting via a
184 novel microtubule-based integration pathway from the nucleus to the cell periphery.
185
186

187 **RESULTS**

188 ***The nuclear LINC protein SUN1 regulates vascular development***

189 The LINC complex is important for cell migration (Chancellor et al., 2010; King et
190 al., 2014; Denis et al., 2021), and blood vessel formation involves extensive endothelial
191 cell migration; thus, we hypothesized that the LINC complex regulates angiogenic
192 sprouting. Because mutations in endothelial cell *LMNA* causative for human
193 cardiovascular disease are associated with expression changes in the LINC protein
194 SUN1 (Chen et al., 2012), and because *Sun1* has not been functionally analyzed in the
195 vascular endothelium *in vivo*, we first asked whether SUN1 is required for vascular
196 development. Utilizing a mouse line carrying a conditional *Sun1* allele that we generated
197 from *Sun1*^{tm1a} "knockout first" mice **(Figure 1-figure supplement 1A-B)**, *Sun1*$^{fl/fl}$ mice
198 were bred to *Sun1*$^{fl/+}$*;Cdh5CreERT2/+* mice to generate *Sun1*^{iECKO} (inducible endothelial
199 cell knockout) mice with both endothelial cell-selective and temporal control over *Sun1*
200 excision. Examination of lung DNA, which is rich in endothelial cells, revealed
201 appropriate excision *in vivo* **(Figure 1-figure supplement 1C)**.

202

203 The retinal vasculature of *Sun1*^{iECKO} pups injected with tamoxifen at P (postnatal
204 day) 1-3 and harvested at P7 had significantly reduced radial expansion relative to
205 littermate controls **(Figure 1A-C, Figure 1-figure supplement 1D)**, consistent with a
206 role for *Sun1* in vascular development. *Sun1*^{iECKO} retinas also had increased density at
207 the vascular front **(Figure 1-figure supplement 1E)**, consistent with defects in
208 sprouting that prevent expansion and thus increase density (Hellström et al., 2007;
209 Ricard et al., 2012; Angulo-Urarte et al., 2018). Since vessel densities in the plexus
210 ahead of arteries and veins exhibit heterogeneity, we measured by area and found
211 increased density in the plexus ahead of both arteries and veins in *Sun1*^{iECKO} retinas

212 **(Figure 1B, D)**. Because adherens junction dynamics regulate vascular sprouting
213 (Sauteur et al., 2014), this mutant phenotype suggested that endothelial cell-cell
214 junctions were affected by loss of *Sun1*. VE-cadherin localization, a readout of junction
215 integrity (Huveneers et al., 2012; Bentley et al., 2014; Wylie et al., 2018; Vion et al.,
216 2020)**,** was significantly less linear and more punctate in *Sun1*^{iECKO} vessels, indicating
217 increased adherens junction turnover and junction instability **(Figure 1E-F)**. Dextran
218 injection was used to functionally evaluate the effects of *Sun1* loss on vascular barrier
219 function *in vivo*, and *Sun1*^{iECKO} mice had increased signal in the surrounding tissue
220 compared to controls **(Figure 1-figure supplement 1F)**, suggesting increased vessel
221 permeability. Together, these data indicate a specific role for SUN1 in angiogenic
222 sprouting and endothelial cell-cell junctions *in vivo*.
223

224 ***Nuclear SUN1 is required for sprouting angiogenesis***

225 *Sun1* loss disrupts vascular development in the postnatal mouse retina **(Figure**
226 **1)**, but this tissue is not amenable to long-term live image analysis. To query dynamic
227 aspects of angiogenic sprouting, which occurs via regulated changes in endothelial
228 adherens junction stability (Sauteur et al., 2014; Angulo-Urarte et al., 2018; Wylie et al.,
229 2018), we utilized a 3D sprouting model (Nakatsu & Hughes, 2008) coupled with
230 temporal image acquisition. Reduced levels of endothelial cell SUN1 via siRNA
231 knockdown (KD) **(Figure 2-figure supplement 1A-B)** led to significantly decreased
232 sprout length and branching **(Figure 2A-C)**, reminiscent of the decreased radial
233 expansion of *Sun1*^{iECKO} retinal vessels described above. SUN1 depletion did not
234 significantly influence the proportion of EdU-labeled or Ki67 stained cells **(Figure 2-**
235 **figure supplement 1C-F)**, indicating that the abnormal sprouting and branching is not
236 downstream of reduced proliferation. Live-cell imaging revealed that control sprouts

237 typically elongated over time, with little retraction once they extended from the bead
238 **(Figure 2D-E, Movie 1)**. In contrast, SUN1 KD sprouts retracted more often, and many
239 mutant sprouts collapsed partially or completely **(Figure 2D-E, Movie 2)**. SUN1 KD
240 sprouts also showed a more diffuse VE-cadherin junction pattern **(Figure 2F-G)**, similar
241 to those of *Sun1*^{iECKO} mice and indicative of over-activated junctions. Thus, SUN1 is
242 required for proper vascular sprout dynamics and morphology, and reduced sprout
243 length and branching are likely downstream of excess sprout retractions and perturbed
244 junctions in SUN1-depleted vessels.
245
246 The LINC complex is important for mechanotransduction in muscle fibers with
247 high mechanical loads (van Ingen & Kirby, 2021), and sprouting angiogenesis is
248 regulated by mechanical forces arising from blood pressure and blood flow (Huang et
249 al., 2003). To determine whether SUN1 also regulates sprouting dynamics under
250 laminar flow *in vivo*, we analyzed embryonic zebrafish using a *Tg(fli:LifeAct-GFP)*
251 reporter that labels the endothelial actin cytoskeleton. Zebrafish have two *Sun1* genes,
252 *sun1a* and *sun1b*; the SUN domain of *sun1b* is more homologous to human *SUN1,* and
253 Sun1b is more highly expressed in cardiovascular tissue, so this gene was chosen for
254 manipulation. Sun1b depletion in zebrafish embryos via morpholino (MO) injection led to
255 significantly increased numbers of shorter endothelial cell filopodia at 33-34 hpf (hours
256 post fertilization) in the inter-segmental vessels (ISVs) that sprout towards and connect
257 to the dorsal longitudinal anastomotic vessel (DLAV) **(Figure 3A-C)**. Like the
258 morphants, fish carrying a point mutation in the *sun1b* gene leading to a premature stop
259 codon (*sun1b*^{sa33109}, see Methods for details) had shorter filopodia, although filopodia
260 numbers were unchanged in the mutant background **(Figure 3D-F)**. Because increased
261 filopodia are typically seen in actively migrating and sprouting endothelial cells

262 (DeLisser, 2011), these changes are consistent with Sun1b regulating endothelial cell
263 activation in developing zebrafish vessels exposed to physiological flow forces.
264
265 Next, *sun1b* morphant fish were imaged from 26-36 hpf to determine the effects
266 of Sun1b depletion on vascular sprouting *in vivo*. In controls, the ISVs sprouted towards
267 the dorsal plane and connected to the DLAV between 32-36 hpf **(Figure 3G-H, Movie**
268 **3)**. In contrast, numerous ISVs either failed to reach the DLAV or made aberrant
269 connections in *sun1b* morphant fish **(Figure 3G-H, Movie 4)**. Staining for the tight
270 junction protein ZO-1 revealed less linear and more abnormally shaped junctions in
271 *sun1b* morphant fish **(Figure 3I-J)**. These results complement the 3D sprouting analysis
272 and show that the nuclear LINC complex protein SUN1 is important in regulating
273 endothelial cell sprouting dynamics and junction morphology under flow forces *in vivo*.
274
275 ***SUN1 stabilizes endothelial cell-cell junctions and regulates barrier function***
276 SUN1 loss or depletion in mouse, zebrafish, and 3D sprouting models resulted in
277 abnormal endothelial cell-cell junctions and sprouting behaviors. Thus, we examined
278 more rigorously the hypothesis that SUN1 regulates endothelial cell junction stability
279 and morphology. Primary human umbilical vein endothelial cells (HUVEC) in confluent
280 monolayers had more serrated cell-cell junctions without altered levels of VE-cadherin
281 protein expression after SUN1 depletion, indicative of activated and destabilized
282 junctions **(Figure 4A, Figure 4-figure supplement 1A-B)**. Activated and destabilized
283 endothelial cell adherens junctions are associated with impaired vascular barrier
284 function, so we measured electrical resistance across endothelial monolayers using
285 Real Time Cell Analysis (RTCA) that provides an impedance value positively correlated
286 with barrier function. SUN1 KD endothelial cells had reduced electrical resistance

287 compared to controls **(Figure 4B-C)**, indicative of impaired barrier function and
288 consistent with the increased dextran permeability *in vivo*. Endothelial cells *in vivo* are
289 exposed to blood flow that remodels endothelial junctions (Seebach et al., 2000; Yang
290 et al., 2020). SUN1 depleted HUVEC exposed to laminar shear stress for 72h elongated
291 and aligned properly, but adherens junctions were more serrated and allowed for
292 significantly more matrix exposure as assessed by a biotin labeling assay (Dubrovskyi
293 et al., 2013) under both static and flow conditions **(Figure 4D-F, Figure 4-figure**
294 **supplement 1C-D)**. These findings support the hypothesis that nuclear SUN1 regulates
295 vascular barrier function via effects on endothelial cell junction stability and morphology.
296
297 Dysfunctional cell-cell junctions can result from abnormal junction formation or
298 the inability of formed junctions to stabilize. To determine how SUN1 functionally
299 regulates endothelial junctions, adherens junctions were disassembled via Ca^{2+}
300 chelation, then reformed upon chelator removal. Junctions were measured using line
301 scans of VE-cadherin intensity along the cell-cell junctions **(Figure 4-figure**
302 **supplement 1E)**, such that junctions with a linear VE-cadherin signal (stable) had a
303 higher value than those with more serrated patterns (destabilized). No significant
304 difference between SUN1 KD and control junctions was seen at early times post-
305 washout, indicating that SUN1 depletion does not affect adherens junction formation
306 **(Figure 4G-H)**. However, later times post-washout revealed a significant increase in
307 serrated junctions and gaps between endothelial cells in SUN1 KD monolayers relative
308 to controls **(Figure 4G-H)**. Consistent with these findings, SUN1 KD endothelial cells
309 also had increased VE-cadherin internalization at steady state, consistent with actively
310 remodeling junctions **(Figure 4-figure supplement 1F-G)**. Thus, SUN1 is not required

311 to form endothelial cell-cell junctions but is necessary for proper junction maturation and
312 stabilization.
313
314 ***SUN1 regulates microtubule localization and dynamics in endothelial cells absent***
315 ***effects on gene transcription***
316 We next considered how SUN1 that resides in the nuclear membrane regulates
317 cell behaviors at the cell periphery. SUN1 may affect cell junctions directly via the
318 cytoskeleton, or SUN1 may indirectly affect junctions downstream of gene expression
319 regulation. Because SUN1 is reported to regulate gene transcription and RNA export in
320 other cell types (Li et al., 2017; May & Carroll, 2018), we asked whether endothelial cell
321 transcriptional profiles were altered by SUN1 depletion. To our surprise, RNASeq
322 analysis of HUVEC under both static and flow conditions revealed essentially no
323 significant changes in RNA profiles except for *SUN1* itself **(Table 1, Figure 5-figure**
324 **supplement 1)**, while in the same experiment we documented extensive expression
325 changes in both up- and down-regulated genes between control HUVEC in static vs.
326 laminar flow conditions, as we and others have shown (Conway et al., 2010; Liu et al.,
327 2021; Maurya et al., 2021; Ruter et al., 2021). These findings are similar to a re-analysis
328 of HeLa cell data (data not shown, (Li et al., 2017)) that revealed few significant
329 changes in gene expression following SUN1 depletion. Thus, although the LINC
330 complex is important for nuclear communication that can affect gene expression, SUN1
331 is not required for this communication in endothelial cells.
332
333 We hypothesized that SUN1 directly regulates endothelial cell junction stability
334 via the cytoskeleton. SUN1 has a functional relationship with the microtubule
335 cytoskeleton (Zhu et al., 2017), and microtubule dynamics regulate endothelial cell-cell

336 junctions (Sehrawat et al., 2008, 2011; Komarova et al., 2012). Thus, we asked whether
337 the observed adherens junction defects following SUN1 depletion resulted from
338 changes in the microtubule cytoskeleton. Microtubule depolymerization via nocodazole
339 treatment phenocopied SUN1 KD and destabilized adherens junctions in control
340 monolayers but did not exacerbate the junction defects seen with SUN1 KD **(Figure 5A-**
341 **B)**. These findings suggest that endothelial cell junction defects are downstream of
342 microtubule perturbations induced by SUN1 depletion.
343
344 We next investigated how SUN1 affects microtubule localization in endothelial
345 cell monolayers and found that significantly fewer microtubules reached the cell
346 periphery or surrounded the nucleus in SUN1 depleted cells **(Figure 5C, E, Figure 5-**
347 **figure supplement 2A-B)**. The changes in peripheral microtubule localization were
348 accompanied by significantly fewer microtubule-junction contacts, while α-tubulin levels
349 around the MTOC were not affected **(Figure 5C, D, F)**. Microtubule dynamics were
350 assessed via tip tracking using mCherry-labeled tip protein EB3, which decorated the
351 microtubule lattice and concentrated at growing microtubule tips **(Figure 5G)**. This
352 labeling pattern can occur with EB overexpression but does not affect growth rate
353 (Komarova et al., 2005), so the decorated lattice was used to assess microtubule
354 catastrophe and shrinkage. Microtubules in SUN1 depleted cells had increased
355 shrinkage rates (a more negative value) coupled with increased catastrophe rate and
356 time spent shrinking **(Figure 5G-K, Movies 5, 6)**, consistent with elevated microtubule
357 depolymerization and impaired microtubule dynamics downstream of SUN1 loss, while
358 the microtubule growth rate was unchanged. Taken together, these results indicate that
359 loss of SUN1 impairs microtubule localization and dynamics, and these changes
360 associate with destabilized endothelial cell junctions.

361 ***SUN1 regulates endothelial cell contractility***

362 Microtubule dynamics communicate with the actin cytoskeleton to regulate cell-
363 cell junctions (Verin et al., 2001; Birukova et al., 2004, 2006), and cellular changes in
364 actomyosin contractility contribute to junction activation (Rauzi et al., 2010; Huveneers
365 et al., 2012). We hypothesized that actomyosin mis-regulation induced by SUN1
366 depletion contributes to endothelial cell junction destabilization and found that SUN1
367 depletion led to ectopic stress fibers, distinct radial actin bundles at the periphery, and
368 increased phosphorylated myosin light chain (ppMLC), consistent with increased
369 actomyosin contractility **(Figure 6-figure supplement 1A-B)**. Pharmacological
370 blockade of myosin-II ATPase rescued the destabilized cell junctions, ectopic stress
371 fibers and radial actin structures seen with SUN1 depletion **(Figure 6A-B, Figure 6-**
372 **figure supplement 1C),** suggesting that SUN1 depletion increases contractility. In
373 contrast, thrombin treatment that induces contractility produced over-activated junctions
374 in controls that phenocopied SUN1 depletion but did not further activate junctions of
375 SUN1 KD cells, indicating that SUN1 loss induces a maximal contractile state **(Figure**
376 **6C-D)**. Taken together, these data indicate that SUN1 loss results in hypercontractility
377 and destabilized endothelial cell-cell junctions.

378

379 ***SUN1 affects endothelial junctions through microtubule-associated Rho GEF-H1***

380 To better understand the link between microtubule dynamics, actomyosin
381 contractility, and junction regulation in endothelial cells, we examined Rho signaling
382 downstream of SUN1 in endothelial cells. SUN1 silencing increases RhoA activity in
383 HeLa cells (Thakar et al., 2017), and pharmacological inhibition of Rho kinase (ROCK)
384 signaling in SUN1 depleted endothelial cells rescued the destabilized endothelial cell-
385 cell junctions **(Figure 6-figure supplement 2A-B)** and prevented the radial actin

386 structures **(Figure 6-figure supplement 1D)**. RhoA signaling and barrier function in
387 endothelial cells is regulated by the microtubule-associated RhoGEF, GEF-H1, which is
388 inactive while bound to microtubules and activated following microtubule
389 depolymerization and release (Krendel et al., 2002; Birukova et al., 2006; Birkenfeld et
390 al., 2008). We hypothesized that the impaired microtubule dynamics and Rho-
391 dependent hypercontractility observed following SUN1 depletion were linked via GEF-
392 H1. Consistent with this idea, GEF-H1 strongly localized to peripheral microtubules in
393 control cells but was significantly less localized and more diffuse in SUN1 depleted
394 endothelial cells **(Figure 6E-F)**. Furthermore, depletion of GEF-H1 in endothelial cells
395 that were also depleted for SUN1 rescued the destabilized cell-cell junctions observed
396 with SUN1 KD alone **(Figure 6G-H, Figure 6-figure supplement 2C)**, showing that
397 GEF-H1 is required to transmit the effects of SUN1 depletion to endothelial cell
398 junctions. Thus, nuclear SUN1 normally promotes microtubule-GEFH1 interactions to
399 regulate actomyosin contractility and endothelial cell-cell junction stability, providing a
400 novel linkage from the LINC complex to endothelial cell junctions via the microtubule
401 cytoskeleton.
402
403 ***SUN1 exerts its effects on endothelial junctions through nesprin-1***
404 Since SUN1 binds nesprins to interact with the cytoskeleton, we considered
405 whether SUN1-nesprin interactions were involved in SUN1 regulation of microtubule
406 dynamics and endothelial cell junction stability. The KASH protein nesprin-1 modulates
407 tight junction protein localization under laminar shear stress (Yang et al., 2020) and
408 regulates microtubule dynamics at the nucleus in muscle syncytia (Gimpel et al., 2017).
409 Co-depletion of SUN1 with nesprin-1 in endothelial cells rescued the effects of SUN1
410 depletion on junction morphology and functional destabilization measured by matrix

411 biotin labeling **(Figure 7A-B, Figure 7-figure supplement 1A)**. This rescue extended to
412 the cytoskeleton, as co-depletion rescued both decreased peripheral microtubule
413 density and microtubule-GEF-H1 contacts seen with SUN1 depletion **(Figure 7-figure**
414 **supplement 1B-E)**. Thus, the LINC complex protein nesprin-1 is required to transmit
415 the effects of SUN1 depletion to endothelial cell junctions.
416

417 **DISCUSSION**

418 The nucleus compartmentalizes and organizes genetic material, but how the
419 nucleus directly communicates with other organelles and the cytoskeleton to regulate
420 cell behaviors is poorly understood. Here, we show for the first time that the nuclear
421 LINC complex protein SUN1 regulates angiogenic sprouting and vascular barrier
422 function via long-distance regulation of endothelial cell-cell junctions *in vivo*, and that
423 these effects go through the microtubule cytoskeleton to regulate microtubule dynamics
424 and actomyosin contractility. Our data is consistent with a model in which endothelial
425 SUN1 stabilizes peripheral microtubules that coordinate activity of the microtubule-
426 associated Rho exchange factor GEF-H1. GEF-H1 becomes activated to stimulate Rho
427 signaling upon release from microtubules, and we posit that peripheral microtubules
428 normally regulate local GEF-H1 activity to maintain appropriate microtubule-junction
429 interactions and actomyosin contractility in endothelial cells, leading to cell-cell junctions
430 that remodel to support angiogenic sprouting and maintain vessel barrier integrity
431 **(Figure 7C)**. Loss of SUN1 reduces peripheral microtubules, resulting in GEF-H1 over-
432 activation, elevated RhoA signaling, and increased contractility, leading to destabilized
433 endothelial cell adherens junctions that impair blood vessel formation and function in
434 fish and mice. The LINC complex is further implicated in endothelial junction regulation
435 by our finding that the KASH protein nesprin-1 is required for the effects of SUN1 loss

436 on microtubules, GEF-H1, and proper junction function. Thus, we describe a specific
437 role for SUN1 as a critical mediator of communication between the endothelial cell
438 nucleus and the cell periphery via microtubule regulation of GEF-H1.
439
440 We show that the LINC complex protein SUN1 is required for endothelial
441 adherens junction stabilization and proper blood vessel formation and function *in vivo*.
442 Although *Sun2* partially compensates for loss of *Sun1* developmentally (Lei et al., 2009;
443 Zhang et al., 2009) and thus may prevent more profound vascular effects, the significant
444 vascular defects in vessels lacking *Sun1* indicate non-redundant functions for SUN1 in
445 vascular development. The adherens junctions of expanding retinal vessels are
446 destabilized in mice lacking endothelial *Sun1*, and this cellular phenotype is
447 accompanied by increased vessel permeability, reduced radial expansion, and
448 increased network density, indicating that destabilized junctions contribute to the vessel
449 network perturbations. Mutations in other genes that affect endothelial cell junction
450 integrity, such as *Smad6*, *Pi3kca*, and *Yap/Taz*, also perturb retinal angiogenesis
451 (Angulo-Urarte et al., 2018; Neto et al., 2018; Wylie et al., 2018). Live-image analysis of
452 active vessel sprouting showed that SUN1 regulates filopodia dynamics and
453 anastomosis in zebrafish and sprout dynamics in mammalian endothelial cell sprouts,
454 and these vessels also had abnormal junctions in the absence of SUN1. Altered sprout
455 dynamics are found in other scenarios where VE-cadherin is absent or abnormal such
456 as Wnt inhibition, loss of VE-cadherin, PI3-kinase inhibition, and excess centrosomes
457 (Sauteur et al., 2014, 2017; Kushner et al., 2016; Angulo-Urarte et al., 2018; Hübner et
458 al., 2018; Buglak et al., 2020). The LINC complex regulates endothelial cell aggregation
459 into tube-like structures in Matrigel (King et al., 2014; Denis et al., 2021), consistent with
460 our findings that highlight a central role for SUN1 in blood vessel formation *in vivo*.

461 Unlike genes encoding components of junctions and signaling effectors, SUN1 functions
462 at significant cellular distances from cell junctions.
463
464 How does SUN1 regulate endothelial cell-cell junctions from a distance? The
465 importance of the LINC complex in transducing signals from the cell periphery and
466 outside the cell to the nucleus to affect nuclear envelope properties and gene
467 transcription is well-studied (Carley et al., 2022); however, how information goes from
468 the nucleus to the cell periphery is less well-understood. Although the LINC complex is
469 clearly important in nucleus-to-cytoplasm communication, most studies have globally
470 manipulated the LINC complex (Zhang et al., 2009; Graham et al., 2018; Carley et al.,
471 2021; Denis et al., 2021), and how individual components contribute is not well-
472 understood. Recently Ueda et al (2022) found that SUN1 regulated focal adhesion
473 maturation in non-endothelial cells *in vitro* via effects on the actin cytoskeleton (Ueda et
474 al., 2022), and we found that SUN1 regulates endothelial cell-cell junctions through
475 microtubules, suggesting that SUN1 is important for signaling from the nucleus to the
476 cell periphery by regulating cytoskeletal organization at several levels. SUN1 is thought
477 to be important in microtubule-associated LINC complex functions (Zhu et al., 2017),
478 and disruption of microtubules or their dynamics destabilizes adherens junctions in both
479 endothelial and non-endothelial cells (Komarova et al., 2012; Vasileva & Citi, 2018).
480 Microtubule plus end dynamics regulate E-cadherin accumulation at epithelial cell
481 adherens junctions (Stehbens et al., 2006), and dynein is thought to anchor microtubule
482 plus ends to junctions via the plus end binding protein EB1 (Ligon et al., 2001; Shaw et
483 al., 2007; Bellett et al., 2009). Microtubule minus ends also regulate protein
484 accumulation at junctions and are anchored to the junction through a complex involving
485 p120 catenin, PLEKHA7, and CAMSAP3 (Meng et al., 2008). Our data show that SUN1

486 depletion impairs both microtubule dynamics and microtubule localization. Specifically,
487 elevated rates of microtubule catastrophe and shrinkage absent changes in growth rate
488 likely account for reduced peripheral microtubule density and microtubule-junction
489 contacts. Endothelial junction destabilization was phenocopied by microtubule
490 depolymerization, consistent with our model that the influence of SUN1 on microtubule
491 dynamics and localization is important for the stabilization of endothelial cell junctions.
492
493 Here we show that SUN1 regulates endothelial cell junctions via the microtubule-
494 regulated Rho activator GEF-H1. GEF-H1 specifically modulates RhoA signaling at
495 endothelial cell adherens junctions to influence VE-cadherin internalization (Juettner et
496 al., 2019). Microtubule depolymerization releases GEF-H1 to activate RhoA signaling
497 and elevate actomyosin contractility (Krendel et al., 2002; Birkenfeld et al., 2008) in non-
498 endothelial cells, while direct manipulation of GEF-H1 via depletion or blockade
499 attenuates agonist-induced endothelial barrier dysfunction (Birukova et al., 2006). Our
500 work revealed that peripheral GEF-H1 localization was more diffuse following
501 endothelial SUN1 silencing, suggesting its activation with SUN1 loss, and Rho-kinase
502 inhibition rescued the SUN1 depletion-induced destabilization of endothelial cell
503 junctions. These findings support that altered microtubule dynamics downstream of
504 SUN1 depletion promote the release and over-activation of peripheral GEF-H1, and this
505 activation destabilizes cell junctions.
506
507 Thus, SUN1 regulation of microtubule dynamics is linked to its regulation of
508 endothelial cell junction stability, although exactly how SUN1 influences microtubule
509 dynamics and function is unclear. SUN1 resides in the nuclear envelope and alters
510 gene transcription in other cell types (Li et al., 2017; May & Carroll, 2018). Our

511 transcriptional analysis of endothelial cells under flow did not reveal significant
512 transcriptome changes with SUN1 depletion, indicating that SUN1 regulation of
513 endothelial junctions occurs via its role in LINC complex interactions with the
514 cytoskeleton. Nesprin-1, a KASH protein that functions in LINC complex-cytoskeletal
515 interactions, is shown here to mediate the effects of SUN1 loss on endothelial junctions,
516 suggesting that SUN1 normally sequesters nesprin-1 to prevent formation of ectopic
517 complexes. Since fewer microtubules surrounded the nucleus in SUN1-depleted
518 endothelial cells, SUN1 may normally prevent abnormal or unstable nesprin-1 LINC
519 complexes that promote microtubule depolymerization, and SUN1 loss allows these
520 complexes to form. SUN1 may compete for nesprin-1 binding with other nuclear
521 envelope proteins that interact with nesprin-1, such as SUN2 or nesprin-3 (Stewart-
522 Hutchinson et al., 2008; Taranum et al., 2012; Yang et al., 2020). This idea is consistent
523 with the finding that SUN1 antagonizes SUN2-based LINC complexes that promote
524 RhoA activity in HeLa cells, although microtubule localization changes were not
525 reported (Thakar et al., 2017).
526
527 Our finding that SUN1 regulates endothelial cell barrier function and blood vessel
528 sprouting has implications for diseases associated with aging, as vascular defects
529 underlie most cardiovascular disease. Children with Hutchinson-Gilford Progeria
530 Syndrome (HGPS) have a mutation in the *LMNA* gene encoding lamin A/C, resulting in
531 accumulation of an abnormal lamin protein called progerin; these patients age rapidly
532 and die in their early to mid-teens from severe atherosclerosis (De Sandre-Giovannoli,
533 2003; Eriksson et al., 2003; Olive et al., 2010). Progerin has increased SUN1 affinity
534 that leads to SUN1 accumulation in HGPS patient cells (Haque et al., 2010; Chen et al.,
535 2012, 2014; Chang et al., 2019). Endothelial cells also accumulate SUN1 in HGPS

536 mouse models (Osmanagic-Myers et al., 2019), and loss of *Sun1* partially rescues
537 progeria phenotypes in mouse models and patient cells (Chen et al., 2012; Chang et al.,
538 2019). Thus, nuclear membrane perturbations affecting SUN1 cause disease, and here
539 we find that nuclear SUN1 regulates microtubules to affect both the microtubule and
540 actin cytoskeletons. These effects are transmitted to endothelial cell-cell junctions far
541 from the site of SUN1 localization to influence endothelial cell behaviors, blood vessel
542 sprouting and barrier function.

543 **MATERIALS & METHODS**

544 ***Microscopy***

545 Unless otherwise stated, all imaging was performed as follows: confocal images
546 were acquired with an Olympus confocal laser scanning microscope and camera
547 (Fluoview FV3000, IX83) using 405nm, 488nm, 561nm, and 640nm lasers and a
548 UPlanSApo 40x silicone-immersion objective (NA 1.25), UPlanSApo 60x oil-immersion
549 objective (NA 1.40), or UPlanSApo 100x oil-immersion objective (NA 1.40). Imaging
550 was performed at RT for fixed samples. Images were acquired with the Olympus
551 Fluoview FV31S-SW software and all image analysis, including Z-stack compression,
552 was performed in Fiji (Linkert et al., 2010; Schindelin et al., 2012). Any adjustments to
553 brightness and contrast were performed evenly for images in an experiment.

554

555 ***Mice***

556 All experiments involving animals were performed with approval from the
557 University of North Carolina, Chapel Hill Institutional Animal Care and Use Committee
558 (IACUC). C57Bl6N-*Sun1*$^{tm1a(EUCOMM)Wtsi}$/CipheOrl mice were obtained from the European
559 Mouse Mutant Archive (EMMA) mouse repository. FlpO-B6N-Albino (Rosa26-FlpO/+)
560 mice were obtained from the UNC Animal Models Core. *Tg(Cdh5-cre/ERT2)1Rha* mice
561 were generated by Dr. Ralf Adams (Sörensen et al., 2009) and obtained from Cancer
562 Research UK. The *Sun1*^{tm1a} allele was identified via genomic PCR to amplify the LacZ
563 insertion (Forward: 5'- ACTATCCCGACCGCCTTACT-3'; Reverse: 5'-
564 TAGCGGCTGATGTTGAACTG-3'). The *Sun1*^{fl} allele was generated by breeding
565 *Sun1*^{tm1a} mice with FlpO-B6N-Albino (Rosa26-FlpO/+) mice to excise the *lacZ* insertion.
566 The *Sun1*^{fl} allele was identified via genomic PCR using the following primers (Forward:
567 5'- GCTCTCTGAAACATGGCTGA-3'; Reverse: 5'- ATCCGGGGTGTTTGGATTAT-3').

568 *Sun1*^{fl} mice were bred to *Tg(Cdh5-cre/ERT2)1Rha* mice to generate
569 *Sun1*$^{fl/fl}$;*Cdh5CreERT2* pups for endothelial-selective and temporally controlled deletion
570 of exon 4 of the *Sun1* gene. The excised *Sun1* allele was identified via genomic PCR on
571 lung tissue using the following primers (Forward: 5'- CTTTTGGGCTGCTCTGTTGT-3';
572 Reverse: 5'- ATCCGGGGTGTTTGGATTAT-3'). PCR genotyping for FlpO and
573 Cdh5CreERT2 mice was performed with the following primers (FlpO: Forward: 5'-
574 TGAGCTTCGACATCGTGAAC -3'; Reverse: 5'-TCAGCATCTTCTTGCTGTGG-3')
575 (Cdh5CreERT2: Forward: 5'- TCCTGATGGTGCCTATCCTC-3'; Reverse: 5'-
576 CCTGTTTTGCACGTTCACCG-3'). Induction of Cre was performed via IP injection of
577 pups at P1, P2, and P3 with 50µl of 1mg/ml tamoxifen (T5648, Sigma) dissolved in
578 sunflower seed oil (S5007, Sigma). Littermates lacking either *Cdh5CreERT2* or the
579 *Sun1*^{fl} allele were used as controls.
580
581 ***Mouse retinas***
582 Tamoxifen-injected mice were sacrificed at P7, eyes were collected, fixed in 4%
583 PFA for 1h at RT, then dissected and stored at 4°C in PBS for up to 2 weeks (Chong et
584 al., 2017). Retinas were permeabilized in 0.5% Triton X-100 (T8787, Sigma) for 1h at
585 RT, blocked for 1h at RT in blocking solution (0.3% Triton X-100, 0.2% BSA (A4503,
586 Sigma), and 5% goat serum (005-000-121, Jackson Immuno)), then incubated with VE-
587 cadherin antibody (anti-mouseCD144, 1:100, 550548, BD Pharmingen) in blocking
588 solution overnight at 4°C. Samples were washed 3X, then incubated with Isolectin B4
589 AlexaFluor 488 (1:100, I21411, ThermoFisher) and goat anti-rat AlexaFluor 647 (1:500,
590 A21247, Life Technologies) for 1h at RT. Retinas were mounted with Prolong Diamond
591 Antifade mounting medium (P36961, Life Technology) and sealed with nail polish.
592 Images were obtained using either a UPlanSApo 10x air objective (NA 0.40) or

593 UPlanSApo 40x silicone-immersion objective (NA 1.25). Percent radial expansion was
594 calculated by dividing the distance from the retina center to the vascular front by the
595 distance from the retina center to the edge of the tissue. Four measurements/retina
596 were averaged. Vascular density was measured by imaging a 350μm x 350μm ROI at
597 the vascular edge. Fiji was used to threshold images, and the vessel area was
598 normalized to the area of the ROI (n=4 ROI/retina, chosen at 2 arteries and 2 veins).
599 Junctions were measured by taking the ratio of the mean intensity of the junction and
600 the mean intensity of the area immediately adjacent to the junction. Mean intensity was
601 measured via line scans in Fiji. 16 junctions/retina were measured.
602

603 ***Retina blood vessel permeability***

604 Tamoxifen-injected mice were anesthetized at P7 in isoflurane for 5 min. The
605 abdomen was opened, and the diaphragm was cut. 100μl of 5mg/ml 10kDa Dextran-
606 Texas Red (D1863, Invitrogen) in PBS was injected into the left ventricle of the heart.
607 Eyes were immediately collected and fixed in 4% PFA for 1h at RT, then dissected and
608 stained as described above. Leak was determined by making a mask of the vessel area
609 using the isolectin channel, then assessing the dextran signal outside the vessel.
610

611 ***3D sprouting angiogenesis assay***

612 The 3D sprouting angiogenesis assay was performed as previously described
613 (Nakatsu & Hughes, 2008; Nesmith et al., 2017). 48h following siRNA knockdown,
614 HUVEC were coated onto cytodex 3 microcarrier beads (17048501, GE Healthcare Life
615 Sciences) and embedded in a fibrin matrix by combining 7μl of 50U/ml thrombin (T7201-
616 500UN, Sigma) with 500μl of 2.2 mg/ml fibrinogen (820224, Fisher) in a 24-well glass-
617 bottomed plate (662892, Grenier Bio). The matrix was incubated for 20 min at RT

618 followed by 20 min at 37°C to allow the matrix to solidify. EGM-2 was then added to
619 each well along with 200µl of normal human lung fibroblasts (CC2512, Lonza) at a
620 concentration of $2x10^5$ cells/ml. At day 7 of sprouting, fibroblasts were removed via
621 trypsin treatment (5X-trypsin for 3min at 37°C), and samples were fixed in 4% PFA for
622 15 min at RT. 0.5% Triton X-100 in DBPS was added to the wells, and incubation was
623 overnight at 4°C. After rinsing 3X in DPBS, samples were blocked (5% goat serum
624 (005-000-121, Jackson Immuno), 1% BSA (A4503, Sigma), and 0.3% Triton X-100
625 (T8787, Sigma)) overnight at 4°C. Samples were rinsed 3X in DPBS then anti-VE-
626 cadherin antibody (1:1000, 2500S, Cell Signaling) in blocking solution was added for
627 24h at 4°C. Samples were rinsed 3X 10 min in 0.5% Tween 20 then washed overnight
628 at 4°C in 0.5% Tween. Samples were rinsed 3X in DPBS, then DAPI (0.3µM,
629 10236276001, Sigma) and AlexaFluor488 Phalloidin (1:50, A12379, Life Technologies)
630 in blocking solution were added to the wells, and incubation was overnight at 4°C prior
631 to rinsing 3X in DPBS. For whole bead analysis, images were acquired in the Z-plane
632 using a UPlanSApo 20x oil-immersion objective (NA 0.58) and processed in Fiji.
633 Average sprout length was measured by tracing each sprout from base (bead) to tip,
634 then averaging lengths per bead. Branching was measured by counting total branch
635 points and normalizing to total sprout length per bead using the AnalyzeSkeleton plugin
636 (Arganda-Carreras et al., 2010). For junctions, images were acquired in the Z-plane
637 using a UPlanSApo 60x oil-immersion objective (NA 1.40). Junctions were measured by
638 taking the ratio of the mean intensity of the junction and the mean intensity of the area
639 immediately adjacent to the junction. Mean intensity was measured via line scans in Fiji.
640

641 Live imaging on HUVEC sprouts was performed between days 4-6.5 of
642 sprouting. Images were acquired on an Olympus VivaView Incubator Fluorescence

643 Microscope with a UPLSAPO 20x objective (NA 0.75) and 0.5x magnification changer
644 (final magnification 20x) with a Hamamatsu Orca R2 cooled CCD camera at 30 min
645 intervals for 60h at 37°C. Images were acquired using the MetaMorph imaging software
646 and analyzed in Fiji. Sprouts were considered to have "retracted" if they regressed
647 towards the bead for at least 3 imaging frames (1.5h).
648
649 ***Zebrafish***
650 All experimental Zebrafish (*Danio rerio*) procedures performed in this study were
651 reviewed and approved by the University of North Carolina Chapel Hill Animal Care and
652 Use Committee. Animals were housed in an AAALAC-accredited facility in compliance
653 with the *Guide for the Care and Use of Laboratory Animals* as detailed on protocols.io
654 (dx.doi.org/10.17504/protocols.io.bg3jjykn). *Tg(fli:LifeAct-GFP)* was a gift from Wiebke
655 Herzog. *sun1b*^{sa33109} mutant fish were obtained from the Zebrafish International
656 Resource Center (ZIRC). For genotyping, the target region of the *sun1b* gene was
657 amplified via genomic PCR using the following primers (Forward: 5'-
658 GGCTGCGTCAGACTCCATTA-3'; Reverse: 5'-TTGAGTTAAACCCAGCGCCT-3'). The
659 amplicon was then sequenced by Sanger sequencing (GENEWIZ) using the forward
660 primer. Morphant fish were obtained by injecting 2.5-5ng of non-targeting (NT) (5'-
661 CCTCTTACCTCAGTTACAATTTATA-3', GeneTools, LLC) or *sun1b* (5'-
662 CGCAGTTTGACCATCAGTTTCTACA-3', GeneTools, LLC) morpholinos into
663 *Tg(fli:LifeAct-GFP)* embryos at the 1-cell stage. Fish were grown in E3 medium at
664 28.5°C to 33-34 hpf.
665

666 ***Zebrafish imaging***

667 Dechorionated embryos were incubated in ice cold 4% PFA at 4°C overnight or
668 RT for 2h. Embryos were permeabilized in 0.5% Triton X-100 in PBST (DPBS + 0.1%
669 Tween 20) for 1 h at RT then blocked (PBST + 0.5% Triton X-100 + 1% BSA + 5% goat
670 serum + 0.01% sodium azide) for 2h at RT. Anti-ZO1 primary antibody (1:500, 33-9100,
671 Thermo Fisher) was added overnight at 4°C. Embryos were rinsed in PBST overnight at
672 4°C. Goat anti-mouse AlexaFluor647 secondary antibody (1:1000, A-21236, Life
673 Technologies) was added overnight at 4°C. Embryos were washed 3X in PBST for 30
674 min then overnight in PBST at 4°C. Embryos were rinsed in PBS and a fine probe was
675 used to de-yolk and a small blade to separate the trunk from the cephalic region.
676 Samples were mounted using Prolong Diamond Antifade mounting medium (P36961,
677 Life Technology) and the coverslip was sealed with petroleum jelly. Imaging was at RT
678 using a UPlanSApo 20x oil-immersion objective (NA 0.58) or a UPlanSApo 60x oil-
679 immersion objective (NA 1.40) with an additional 3x magnification, for a total
680 magnification of 180x. Filopodia length was measured by drawing a line from the
681 filopodia base to the tip. Filopodia number was measured by counting the number of
682 filopodia and normalizing to the total vessel length. Filopodia in at least 3 areas per fish
683 were measured. Junctions were analyzed by drawing a line along the junction then
684 normalizing to the shortest distance between the two ends of the junction. At least 3
685 junctions were measured per fish.

686

687 For live imaging of zebrafish, fish were dechorionated and then anesthetized with
688 1x Tricaine in E3 for 5 min. Fish were embedded in 0.5% agarose in 1x Tricaine-E3
689 medium on a glass-bottomed plate in a stage-top incubator (TOKAI HIT, WSKM) at
690 28.5°C. Images were acquired using a UPlanSApo 40x air objective (NA 0.95) every

691 15min for 10-15h. ISVs that did not reach the DLAV or connected at non-consistent
692 intervals were considered to have a missing or aberrant DLAV connection if at least 1
693 ISV posterior to the scored ISV made a normal connection.
694
695 ***Cell culture***
696 HUVEC (C2519A, Lonza) were cultured in EBM-2 (CC-3162, Lonza)
697 supplemented with the Endothelial Growth Medium (EGM-2) bullet kit (CC-3162, Lonza)
698 and 1x antibiotic-antimycotic (Gibco). Normal human lung fibroblasts (CC2512, Lonza)
699 were cultured in DMEM (Gibco) with 10% fetal bovine serum (FBS) and 1x antibiotic-
700 antimycotic (Gibco). All cells were maintained at 37°C and 5% CO_2. For contractility
701 inhibition experiments, HUVEC were treated with 10μM (-) Blebbistatin (B0560-1MG,
702 Sigma) for 15 min at 37°C or 10μM Y-27632 (10187-694, VWR) for 30 min at 37°C then
703 immediately fixed in 4% PFA. For induction of contractility, HUVEC were treated with
704 0.5U/ml thrombin (T7201-500UN, Sigma) for 10 min at 37°C. For microtubule
705 depolymerization, HUVEC were treated with 10μM nocodazole (M1404, Sigma) for 20
706 min at 37°C then immediately fixed in methanol.
707
708 ***siRNA knockdown***
709 HUVEC were transfected with non-targeting siRNA (NT, #4390847, Life
710 Technologies), SUN1 siRNA #1 (439240, #s23630, Life Technologies), SUN1 siRNA #2
711 (439240, #s23629, Life Technologies), GEF-H1 siRNA (439240, #s17546, Life
712 Technologies), and/or nesprin-1 siRNA (M-014039-02-0005, Dharmacon) using
713 Lipofectamine 2000 (11668027, Invitrogen) or Lipofectamine 3000 (L3000015,
714 ThermoFisher). siRNA at 0.48μM in Opti-MEM (31985-070, Gibco) and a 1:20 dilution of
715 Lipofectamine in Opti-MEM were incubated separately at RT for 5 min, then combined

716 and incubated at RT for 15 min. HUVEC were transfected at ~80% confluency with
717 siRNA at 37°C for 24h, then recovered in EGM-2 for an additional 24h. HUVEC were
718 seeded onto glass chamber slides coated with 5μg/ml fibronectin (F2006-2MG, Sigma)
719 for experiments.
720
721 ***RNA sequencing and analysis***
722 RNA was extracted using TRIzol (15596018, Invitrogen) from 3 biological
723 replicates (independent experiments) of HUVEC under static or homeostatic laminar
724 flow (15d/cm^2, 72hr) conditions, and KAPA mRNA HyperPrep Kit (7961901001, Roche)
725 was used to prepare stranded libraries for sequencing (NovaSeq S1). 2–3 × 10^7
726 50-bp paired-end reads per sample were obtained and mapped to human genome
727 GRCh38 downloaded from https://support.10xgenomics.com/single-cell-gene-
728 expression/software/pipelines/latest/advanced/references with STAR using default
729 settings (Dobin et al., 2013). Mapping rate was over 80% for all samples, and gene
730 expression was determined with Htseq-count using the union mode
731 (https://htseq.readthedocs.io/en/master/) (Putri et al., 2022). Differential expression
732 analysis was performed with DESeq2 (Love et al., 2014) using default settings in R, and
733 lists of differentially expressed genes were obtained (p adjusted < 0.1).
734
735 ***Immunofluorescence staining***
736 For experiments visualizing microtubules, HUVEC were fixed in ice-cold
737 methanol for 10 min at 4°C. For all other experiments, HUVEC were fixed with 4% PFA
738 for 10 min at RT and permeabilized with 0.1% Triton X-100 (T8787, Sigma) for 10 min
739 at RT. Fixed HUVEC were blocked for 1h at RT in blocking solution (5% FBS, 2X
740 antibiotic-antimycotic (Gibco), 0.1% sodium azide (s2002-100G, Sigma) in DPBS). Cells

741 were incubated in primary antibody overnight at 4°C, then washed 3X for 5 min in
742 DPBS. Secondary antibody and DRAQ7 (1:1000, ab109202, Abcam), DAPI (0.3μM,
743 10236276001, Sigma), and/or AlexaFluor488 Phalloidin (1:100, A12379, Life
744 Technologies) were added for 1h at RT followed by 3X washes for 10 min each in
745 DPBS. Slides were mounted with coverslips using Prolong Diamond Antifade mounting
746 medium (P36961, Life Technology) and sealed with nail polish. Primary and secondary
747 antibodies were diluted in blocking solution. The following primary antibodies were
748 used: anti-VE-cadherin (1:500, 2500S, Cell Signaling), anti-SUN1 (1:500, ab124770,
749 Abcam), anti-Ki67 (1:500, ab15580, Abcam), anti-phospho-myosin light chain 2
750 (Thr18/Ser19) (1:500, 3674S, Cell Signaling), anti-alpha-tubulin (1:500, 3873S, Cell
751 Signaling), anti-GEF-H1 (1:500, ab155785, Abcam), and anti-SYNE1 (1:500,
752 HPA019113, Atlas Antibodies). The following secondary antibodies from Life
753 Technologies were used: goat anti-mouse AlexaFluor 488 (1:500, A11029), goat anti-
754 rabbit AlexaFluor 594 (1:500, A11037), goat anti-mouse 647 (1:500, A21236), and goat
755 anti-rabbit 647 (1:500, A21245).
756
757 ***Western blotting***
758 Cells were scraped into RIPA buffer with protease/phosphatase inhibitor (5872S,
759 Cell Signaling) then centrifuged at 13000 rpm at 4°C for 20 min. Lysate was reduced in
760 sample loading buffer and dithiothreitol (R0861, Thermo Fisher) and boiled for 10 min at
761 100°C. Samples were stored at -20°C until use. 10μg of sample were run on a 10%
762 stain-free polyacrylamide gel (161-0183, BioRad) then transferred onto a PVDF
763 membrane on ice for 1.5h. Membranes were blocked in OneBlock (20-313,
764 Prometheus) for 1 h at RT then washed 3X in PBST. Anti-GEF-H1 (1:1000, ab155785,
765 Abcam), anti-VE-cadherin (1:14,000, 2500S, Cell Signaling), or anti-GAPDH (1:5000,

766 97166S, Cell Signaling) was added overnight at 4°C. Membranes were washed 3X in
767 PBST then donkey anti-rabbit HRP secondary antibody (1:10,000, A16035, Thermo
768 Fisher) was added for 1h at RT. Immobilon Forte HRP Substrate (WBLUF0100,
769 Millipore Sigma) was added for 30 sec. Blots were exposed for 8 sec.
770
771 ***EdU labeling***
772 HUVEC were labeled with EdU using the Click-It EdU Kit 488 (Invitrogen,
773 C10337) and fixed according to the manufacturer's instructions. Cells positive for EdU
774 labeling were counted and compared to total cell number to obtain percent positive.
775
776 ***Junction analysis***
777 Endothelial cell adherens junctions were quantified in monolayers using Fiji to
778 generate 15μm line scans of VE-cadherin signal parallel to the cell junctions. VE-
779 cadherin signal was integrated to obtain the area under the curve. Linear junctions with
780 consistent VE-cadherin signal thus had a large area under the curve, while more
781 serrated junctions had reduced area under the curve **(Fig S3e)**. Measurements were
782 performed on at least 9 cells per field of view, with 3-6 fields of view per condition.
783
784 ***Real time cell analysis (RTCA)***
785 Barrier function was assessed using the xCELLigence Real-Time Cell Analyzer
786 (RTCA, Acea Biosciences/Roche Applied Science) to measure electrical impedance
787 across HUVEC monolayers seeded onto microelectrodes. HUVEC were seeded to
788 confluency on the microelectrodes of the E-plate (E-plate 16, Roche Applied Science).
789 Electrical impedance readings were taken every 2 min for 5h. The percent change in

790 cell index was obtained at the 5h timepoint using the following formula: (Cell $Index_{SUN1}$-
791 Cell $Index_{NT}$)/ABS(Cell $Index_{NT}$).
792
793 ***Flow experiments***
794 Flow experiments were performed using an Ibidi pump system (10902, Ibidi) as
795 described (Ruter et al., 2021). HUVEC were seeded onto fibronectin coated Ibidi slides
796 (either μ-Slide I Luer I 0.4 mm (80176, Ibidi) or μ-Slide Y-shaped (80126, Ibidi) in flow
797 medium (EBM-2 with 10% FBS and 1x Antibiotic-antimycotic). HUVEC were exposed to
798 laminar shear stress for 30 min at 5 dyn/cm2, followed by 30 min at 10 dyn/cm2, and
799 finally for 72 h at 15 dyn/cm2. Alignment was measured by taking the ratio of the
800 longitudinal axis to the transverse axis relative to the flow vector. At least 10 cells were
801 measured per condition per experiment. Vascular permeability *in vitro* was determined
802 using the biotin matrix labeling assay as described below.
803
804 ***Biotin matrix labeling assay***
805 Labeling of biotinylated matrix was assessed as described (Dubrovskyi et al.,
806 2013). Briefly, fibronectin was biotinylated by incubating 0.1mg/mL fibronectin with
807 0.5mM EZ-Link Sulfo-NHS-LC-Biotin (A39257, ThermoFisher) for 30 min at RT. Glass
808 chamber slides were coated with 5μg/ml biotinylated-fibronectin and HUVEC were
809 seeded on top. At confluency, HUVEC were treated with 25μg/mL Streptavidin-488
810 (S11223, Invitrogen) for 3 min then immediately fixed. For quantification, Fiji was used
811 to threshold the streptavidin signal, and the streptavidin area was measured and
812 normalized for total area for at least 3 fields of view per experiment.
813

814 ***Junction reformation assay***

815 The EDTA junction reformation assay was performed as previously described
816 (Wright et al., 2015). Briefly, HUVEC were treated with 3mM EDTA (EDS-100G, Sigma-
817 Aldrich) for 1h at 37°C. EDTA was then washed out 3X with DPBS, incubation at 37°C
818 in EGM-2 was continued, and cells were fixed at 0 min, 20 min, 40 min, and 60 min
819 intervals.

820

821 ***VE-cadherin internalization***

822 VE-cadherin internalization was performed as described (Wylie et al., 2018).
823 Briefly, HUVEC were plated on 5µg/ml fibronectin and grown to confluency. After
824 overnight serum starvation (Opti-MEM (31985-070, Gibco) supplemented with 1% FBS
825 (F2442, Sigma), and 1x antibiotic-antimycotic (Gibco)), cells were washed with pre-
826 chilled PBS+ (14040182, ThermoFisher) on ice at 4°C, then incubated in ice-cold
827 blocking solution (EBM-2 (CC-3162, Lonza) supplemented with 0.5% BSA (A4503,
828 Sigma)) for 30 min at 4°C. HUVEC were then incubated with VE-cadherin BV6 antibody
829 (1:100, ALX-803-305-C100, Enzo) in blocking solution for 2h on ice at 4°C. Following
830 VE-cadherin labeling, cells were washed with PBS+ then incubated in pre-warmed
831 internalization medium (EBM-2) at 37°C for 1h. Finally, HUVEC were incubated in acid
832 wash (0.5M NaCl/0.2M acetic acid) for 4 min at 4°C to remove remaining labeled VE-
833 cadherin on the cell surface, then washed with PBS+ and fixed. For quantification,
834 internalized VE-cadherin area was measured in Fiji, then normalized to total cell area
835 for at least 9 cells per experiment.

836

837 ***Microtubule analysis***

838 For nuclear microtubule analysis, an ROI was drawn in Fiji over the nucleus. Fiji
839 was used to threshold α-tubulin signal, and the area of the signal was measured within
840 the ROI. This was performed on 8 cells per field of view, with 3-6 fields per condition per
841 experiment. For high-resolution microtubule analysis, high-resolution confocal images
842 were acquired with a Zeiss 880 Confocal with AiryScan FAST microscope with GaAsP
843 detector and camera (Zeiss) using a Plan-Apo 63x oil immersion objective (NA 1.40)
844 and 488nm and 561nm lasers. Imaging was performed at RT, and images were
845 acquired with the Zeiss 880 software and with the AiryScan detector. Images were then
846 processed with AiryScan. All image analysis, including Z-stack compression, was
847 performed in Fiji. For microtubule density, an ROI was drawn at the MTOC and the cell
848 periphery. Fiji was used to threshold α-tubulin signal, and the area of the signal was
849 measured within the ROI. This was performed on at least 10 cells per condition per
850 experiment. For junction analysis, the number of contacts between α-tubulin and VE-
851 cadherin were counted and normalized to the junction length. At least 15 junctions were
852 measured per condition per experiment.

853

854 ***Microtubule tip tracking***

855 HUVEC were infected with an EB3-mCherry Lentivirus (Kushner et al., 2014) for
856 24h to visualize microtubule comets. Following infection, HUVEC were incubated with
857 siRNAs for NT or SUN1. For live imaging, cells were incubated at 37°C in a stage-top
858 incubator (TOKAI HIT, WSKM). Images were acquired on an Andor XD spinning disk
859 confocal microscope based on a CSU-X1 Yokogawa head with an Andor iXon 897 EM-
860 CCD camera. A 561nm laser and FF01-607/36 emission filter were used. Images were
861 acquired with a 470ms exposure and 32ms readout time for 2 min (240 frames) using a

862 UPlanSApo 60x silicone-oil immersion objective (NA 1.30) and Metamorph software.
863 Microtubules at the cell periphery were tracked using the Manual Tracking plugin in Fiji
864 and were tracked for at least 60 frames (30 sec). Track information was acquired from
865 the x and y coordinates using a custom algorithm in Visual Basic in Excel provided by
866 Dan Buster at the University of Arizona. 10 microtubule tracks were measured per cell.
867

868 ***GEF-H1 analysis***

869 For GEF-H1 localization analysis, an ROI was drawn at the periphery of the cell,
870 and the α-tubulin signal was used to create a mask. Mean signal intensity was then
871 measured for GEF-H1 within the α-tubulin mask and outside of it, and a ratio was taken.
872 At least 9 cells were analyzed per condition per experiment.
873

874 ***Statistics***

875 Student's two-tailed unpaired *t*-test was used to determine statistical significance
876 in experiments with 2 groups and one-way ANOVA with Tukey's multiple comparisons
877 test was used in experiments with 3 groups. For thrombin, blebbistatin, Y-27632, and
878 nocodazole experiments, two-way ANOVA with Tukey's multiple comparisons test was
879 used to determine statistical significance. X^2 was used for categorical data. For box and
880 whisker plots, boxes represent the upper quartile, lower quartile, and median; whiskers
881 represent the minimum and maximum values. Statistical tests and graphs were made
882 using the Prism 9 software (GraphPad Software).
883

884 ***Data availability***

885 The RNA-seq data that support the findings of this study are available in the
886 Gene Expression Omnibus (GEO) under the accession number GSE213099.

887

888 **ACKNOWLEGMENTS**

889 We thank Michelle Altemara and staff at the Zebrafish Aquaculture Core and
890 Kaitlyn Quigley for fish room support, Aaron Friedman and Caroline Crater for mouse
891 room support, and Yosuke Mukouyama, Nick Buglak, and Bautch Lab members for
892 critical discussion and feedback. We also thank Dan Buster for the software used in
893 microtubule tip tracking experiments and Angelika Noegel for sharing RNASeq data with
894 us. Airy Scan imaging was performed at the UNC Hooker Imaging Core Facility and
895 microtubule tip tracking imaging was performed with Pablo Ariel at the UNC Microscopy
896 Services Laboratory, supported in part by P30 CA016086 Cancer Center Core Support
897 Grant to the UNC Lineberger Comprehensive Cancer Center.

898

899 **AUTHOR CONTRIBUTIONS**

900 Danielle B Buglak (DBB) and Victoria L Bautch (VLB) conceptualized the work;
901 DBB, Ariel L Gold (ALG), Allison P Marvin (APM), Shea N Ricketts (SNR), Molly R
902 Kulikauskas (MRK), Andrew Burciu (AB), Karina Kinghorn (KK), Morgan Oatley (MO),
903 Natalie T Tanke (NTT), Pauline Bougaran (PB), and Bryan N Johnson (BNJ) performed
904 and analyzed experiments; Ziqing Liu (ZL) analyzed RNASeq data; DBB and VLB wrote
905 and edited the manuscript; Celia E Shiau (CES) provided oversight on zebrafish
906 experiments; Stephen L Rogers (SLR) provided oversight and discussion on
907 microtubule and GEF-H1 experiments; VLB provided study supervision and oversight.

908

909 **FUNDING**

910 This work was supported by grants from the National Institutes of Health (R35
911 HL139950 to VLB), the Integrated Vascular Biology Training Grant (5T32HL069768-17,

912 DBB), and an American Heart Association Predoctoral Fellowship (19PRE34380887 to
913 DBB).

914

915 **DECLARATION OF INTERESTS:** None.

916

917

REFERENCES

Abu Taha, A., & Schnittler, H.-J. (2014). Dynamics between actin and the VE-cadherin/catenin complex: novel aspects of the ARP2/3 complex in regulation of endothelial junctions. Cell Adhesion & Migration, *8*(2), 125–135. https://doi.org/10.4161/cam.28243

Angulo-Urarte, A., Casado, P., Castillo, S. D., Kobialka, P., Kotini, M. P., Figueiredo, A. M., Castel, P., Rajeeve, V., Milà-Guasch, M., Millan, J., et al. (2018). Endothelial cell rearrangements during vascular patterning require PI3-kinase-mediated inhibition of actomyosin contractility. Nature Communications, *9*(1), 4826. https://doi.org/10.1038/s41467-018-07172-3

Anno, T., Sakamoto, N., & Sato, M. (2012). Role of nesprin-1 in nuclear deformation in endothelial cells under static and uniaxial stretching conditions. Biochemical and Biophysical Research Communications, *424*(1), 94–99. https://doi.org/10.1016/j.bbrc.2012.06.073

Arganda-Carreras, I., Fernández-González, R., Muñoz-Barrutia, A., & Ortiz-De-Solorzano, C. (2010). 3D reconstruction of histological sections: Application to mammary gland tissue. Microscopy Research and Technique, *73*(11), 1019–1029. https://doi.org/10.1002/jemt.20829

Banerjee, I., Zhang, J., Moore-Morris, T., Pfeiffer, E., Buchholz, K. S., Liu, A., Ouyang, K., Stroud, M. J., Gerace, L., Evans, S. M., et al. (2014). Targeted ablation of nesprin 1 and nesprin 2 from murine myocardium results in cardiomyopathy, altered nuclear morphology and inhibition of the biomechanical gene response. PLoS Genetics, *10*(2), e1004114. https://doi.org/10.1371/journal.pgen.1004114

Bautch, V. L., & Caron, K. M. (2015). Blood and lymphatic vessel formation. Cold Spring Harbor Perspectives in Biology, *7*(3), a008268. https://doi.org/10.1101/cshperspect.a008268

Bellett, G., Carter, J. M., Keynton, J., Goldspink, D., James, C., Moss, D. K., & Mogensen, M. M. (2009). Microtubule plus-end and minus-end capture at adherens junctions is involved in the assembly of apico-basal arrays in polarised epithelial cells. Cell Motility and the Cytoskeleton, *66*(10), 893–908. https://doi.org/10.1002/cm.20393

Bentley, K., Franco, C. A., Philippides, A., Blanco, R., Dierkes, M., Gebala, V., Stanchi, F., Jones, M., Aspalter, I. M., Cagna, G., et al. (2014). The role of differential VE-cadherin dynamics in cell rearrangement during angiogenesis. Nature Cell Biology, *16*(4), 309–321.

Birkenfeld, J., Nalbant, P., Yoon, S.-H., & Bokoch, G. M. (2008). Cellular functions of GEF-H1, a microtubule-regulated Rho-GEF: is altered GEF-H1 activity a crucial determinant of disease pathogenesis? Trends in Cell Biology, *18*(5), 210–219. https://doi.org/10.1016/j.tcb.2008.02.006

958 Birukova, A. A., Adyshev, D., Gorshkov, B., Bokoch, G. M., Birukov, K. G., & Verin, A.
959 D. (2006). GEF-H1 is involved in agonist-induced human pulmonary endothelial
960 barrier dysfunction. American Journal of Physiology. Lung Cellular and Molecular
961 Physiology, *290*(3), L540-8. https://doi.org/10.1152/ajplung.00259.2005

962 Birukova, A. A., Liu, F., Garcia, J. G. N., & Verin, A. D. (2004). Protein kinase A
963 attenuates endothelial cell barrier dysfunction induced by microtubule disassembly.
964 American Journal of Physiology. Lung Cellular and Molecular Physiology, *287*(1),
965 L86-93. https://doi.org/10.1152/ajplung.00441.2003

966 Blum, Y., Belting, H.-G., Ellertsdottir, E., Herwig, L., Lüders, F., & Affolter, M. (2008).
967 Complex cell rearrangements during intersegmental vessel sprouting and vessel
968 fusion in the zebrafish embryo. Developmental Biology, *316*(2), 312–322.
969 https://doi.org/10.1016/j.ydbio.2008.01.038

970 Buglak, D. B., Kushner, E. J., Marvin, A. P., Davis, K. L., & Bautch, V. L. (2020). Excess
971 centrosomes disrupt vascular lumenization and endothelial cell adherens junctions.
972 Angiogenesis, *23*(4), 567–575. https://doi.org/10.1007/s10456-020-09737-7

973 Capell, B. C., & Collins, F. S. (2006). Human laminopathies: nuclei gone genetically
974 awry. Nature Reviews. Genetics, *7*(12), 940–952. https://doi.org/10.1038/nrg1906

975 Carley, E., King, M. C., & Guo, S. (2022). Integrating mechanical signals into cellular
976 identity. Trends in Cell Biology, *32*(8), 669–680.
977 https://doi.org/10.1016/j.tcb.2022.02.006

978 Carley, E., Stewart, R. M., Zieman, A., Jalilian, I., King, D. E., Zubek, A., Lin, S.,
979 Horsley, V., & King, M. C. (2021). The LINC complex transmits integrin-dependent
980 tension to the nuclear lamina and represses epidermal differentiation. ELife, *10*.
981 https://doi.org/10.7554/eLife.58541

982 Carmeliet, P., & Jain, R. K. (2011). Principles and mechanisms of vessel normalization
983 for cancer and other angiogenic diseases. Nature Reviews Drug Discovery, *10*,
984 417–427.

985 Carmeliet, P., Lampugnani, M. G., Moons, L., Breviario, F., Compernolle, V., Bono, F.,
986 Balconi, G., Spagnuolo, R., Oosthuyse, B., Dewerchin, M., et al. (1999). Targeted
987 deficiency or cytosolic truncation of the VE-cadherin gene in mice impairs VEGF-
988 mediated endothelial survival and angiogenesis. Cell, *98*(147–157).

989 Chancellor, T. J., Lee, J., Thodeti, C. K., & Lele, T. (2010). Actomyosin tension exerted
990 on the nucleus through nesprin-1 connections influences endothelial cell adhesion,
991 migration, and cyclic strain-induced reorientation. Biophysical Journal, *99*(1), 115–
992 123. https://doi.org/10.1016/j.bpj.2010.04.011

993 Chang, W., Wang, Y., Luxton, G. W. G., Östlund, C., Worman, H. J., & Gundersen, G.
994 G. (2019). Imbalanced nucleocytoskeletal connections create common polarity
995 defects in progeria and physiological aging. Proceedings of the National Academy
996 of Sciences of the United States of America, *116*(9), 3578–3583.
997 https://doi.org/10.1073/pnas.1809683116

998 Chen, C.-Y., Chi, Y.-H., Mutalif, R. A., Starost, M. F., Myers, T. G., Anderson, S. A.,
999 Stewart, C. L., & Jeang, K.-T. (2012). Accumulation of the Inner Nuclear Envelope
1000 Protein Sun1 Is Pathogenic in Progeric and Dystrophic Laminopathies. Cell, *149*(3),
1001 565–577. https://doi.org/10.1016/j.cell.2012.01.059

1002 Chen, Z.-J., Wang, W.-P., Chen, Y.-C., Wang, J.-Y., Lin, W.-H., Tai, L.-A., Liou, G.-G.,
1003 Yang, C.-S., & Chi, Y.-H. (2014). Dysregulated interactions between lamin A and
1004 SUN1 induce abnormalities in the nuclear envelope and endoplasmic reticulum in
1005 progeric laminopathies. Journal of Cell Science, *127*(Pt 8), 1792–1804.
1006 https://doi.org/10.1242/jcs.139683

1007 Chong, D. C., Yu, Z., Brighton, H. E., Bear, J. E., & Bautch, V. L. (2017). Tortuous
1008 Microvessels Contribute to Wound Healing via Sprouting Angiogenesis.
1009 Arteriosclerosis, Thrombosis, and Vascular Biology, *37*(10), 1903–1912.
1010 https://doi.org/10.1161/ATVBAHA.117.309993

1011 Claesson-Welsh, L. (2015). Vascular permeability--the essentials. Upsala Journal of
1012 Medical Sciences, *120*(3), 135–143.
1013 https://doi.org/10.3109/03009734.2015.1064501

1014 Claesson-Welsh, L., Dejana, E., & McDonald, D. M. (2021). Permeability of the
1015 Endothelial Barrier: Identifying and Reconciling Controversies. Trends in Molecular
1016 Medicine, *27*(4), 314–331. https://doi.org/10.1016/j.molmed.2020.11.006

1017 Conway, D. E., Williams, M. R., Eskin, S. G., & McIntire, L. V. (2010). Endothelial cell
1018 responses to atheroprone flow are driven by two separate flow components: low
1019 time-average shear stress and fluid flow reversal. American Journal of Physiology.
1020 Heart and Circulatory Physiology, *298*(2), H367-74.
1021 https://doi.org/10.1152/ajpheart.00565.2009

1022 De Sandre-Giovannoli, A. (2003). Lamin A Truncation in Hutchinson-Gilford Progeria.
1023 Science, *300*(5628), 2055–2055. https://doi.org/10.1126/science.1084125

1024 Dejana, E. (2004). Endothelial cell-cell junctions: happy together. Nature Reviews.
1025 Molecular Cell Biology, *5*(4), 261–270. https://doi.org/10.1038/nrm1357

1026 Dejana, E., & Vestweber, D. (2013). The role of VE-cadherin in vascular morphogenesis
1027 and permeability control. Progress in Molecular Biology and Translational Science,
1028 *116*, 119–144. https://doi.org/10.1016/B978-0-12-394311-8.00006-6

1029 DeLisser, H. M. (2011). Modulators of endothelial cell filopodia: PECAM-1 joins the club.
1030 Cell Adhesion & Migration, *5*(1), 37–41. https://doi.org/10.4161/cam.5.1.13575

1031 Denis, K. B., Cabe, J. I., Danielsson, B. E., Tieu, K. V, Mayer, C. R., & Conway, D. E.
1032 (2021). The LINC complex is required for endothelial cell adhesion and adaptation
1033 to shear stress and cyclic stretch. Molecular Biology of the Cell, mbcE20110698.
1034 https://doi.org/10.1091/mbc.E20-11-0698

1035 Dobin, A., Davis, C. A., Schlesinger, F., Drenkow, J., Zaleski, C., Jha, S., Batut, P.,
1036 Chaisson, M., & Gingeras, T. R. (2013). STAR: ultrafast universal RNA-seq aligner.

1037 Bioinformatics (Oxford, England), *29*(1), 15–21.
1038 https://doi.org/10.1093/bioinformatics/bts635

1039 Dubrovskyi, O., Birukova, A. A., & Birukov, K. G. (2013). Measurement of local
1040 permeability at subcellular level in cell models of agonist- and ventilator-induced
1041 lung injury. Laboratory Investigation; a Journal of Technical Methods and
1042 Pathology, *93*(2), 254–263. https://doi.org/10.1038/labinvest.2012.159

1043 Eriksson, M., Brown, W. T., Gordon, L. B., Glynn, M. W., Singer, J., Scott, L., Erdos, M.
1044 R., Robbins, C. M., Moses, T. Y., Berglund, P., et al. (2003). Recurrent de novo
1045 point mutations in lamin A cause Hutchinson-Gilford progeria syndrome. Nature,
1046 *423*(6937), 293–298. https://doi.org/10.1038/nature01629

1047 Esser, S., Lampugnani, M. G., Corada, M., Dejana, E., & Risau, W. (1998). Vascular
1048 endothelial growth factor induces VE-cadherin tyrosine phosphorylation in
1049 endothelial cells. Journal of Cell Science, *111 (Pt 1*, 1853–1865. Retrieved from
1050 http://www.ncbi.nlm.nih.gov/pubmed/9625748

1051 Fridolfsson, H. N., Ly, N., Meyerzon, M., & Starr, D. A. (2010). UNC-83 coordinates
1052 kinesin-1 and dynein activities at the nuclear envelope during nuclear migration.
1053 Developmental Biology, *338*(2), 237–250.
1054 https://doi.org/10.1016/j.ydbio.2009.12.004

1055 Gimpel, P., Lee, Y. L., Sobota, R. M., Calvi, A., Koullourou, V., Patel, R., Mamchaoui,
1056 K., Nédélec, F., Shackleton, S., Schmoranzer, J., et al. (2017). Nesprin-1α-
1057 Dependent Microtubule Nucleation from the Nuclear Envelope via Akap450 Is
1058 Necessary for Nuclear Positioning in Muscle Cells. Current Biology : CB, *27*(19),
1059 2999-3009.e9. https://doi.org/10.1016/j.cub.2017.08.031

1060 Graham, D. M., Andersen, T., Sharek, L., Uzer, G., Rotherberg, K., Hoffman, B. D.,
1061 Rubin, J., Balland, M., Bear, J. E., & Burridge, K. (2018). Enucleated cells reveal
1062 differential roles of the nucleus in cell migration, polarity, and mechanotransduction.
1063 Journal of Cell Biology, jcb.201706097.

1064 Guilluy, C., Osborne, L. D., Van Landeghem, L., Sharek, L., Superfine, R., Garcia-Mata,
1065 R., & Burridge, K. (2014). Isolated nuclei adapt to force and reveal a
1066 mechanotransduction pathway in the nucleus. Nature Cell Biology, *16*(4), 376–381.
1067 https://doi.org/10.1038/ncb2927

1068 Han, Y., Wang, L., Yao, Q.-P., Zhang, P., Liu, B., Wang, G.-L., Shen, B.-R., Cheng, B.,
1069 Wang, Y., Jiang, Z.-L., et al. (2015). Nuclear envelope proteins Nesprin2 and
1070 LaminA regulate proliferation and apoptosis of vascular endothelial cells in
1071 response to shear stress. Biochimica et Biophysica Acta, *1853*(5), 1165–1173.
1072 https://doi.org/10.1016/j.bbamcr.2015.02.013

1073 Haque, F., Lloyd, D. J., Smallwood, D. T., Dent, C. L., Shanahan, C. M., Fry, A. M.,
1074 Trembath, R. C., & Shackleton, S. (2006). SUN1 interacts with nuclear lamin A and
1075 cytoplasmic nesprins to provide a physical connection between the nuclear lamina
1076 and the cytoskeleton. Molecular and Cellular Biology, *26*(10), 3738–3751.

1077 Haque, F., Mazzeo, D., Patel, J. T., Smallwood, D. T., Ellis, J. A., Shanahan, C. M., &
1078 Shackleton, S. (2010). Mammalian SUN protein interaction networks at the inner
1079 nuclear membrane and their role in laminopathy disease processes. The Journal of
1080 Biological Chemistry, *285*(5), 3487–3498. https://doi.org/10.1074/jbc.M109.071910

1081 Hellström, M., Phng, L.-K., Hofmann, J. J., Wallgard, E., Coultas, L., Lindblom, P., Alva,
1082 J., Nilsson, A.-K., Karlsson, L., Gaiano, N., et al. (2007). Dll4 signalling through
1083 Notch1 regulates formation of tip cells during angiogenesis. Nature, *445*(7129),
1084 776–780. https://doi.org/10.1038/nature05571

1085 Huang, C., Sheikh, F., Hollander, M., Cai, C., Becker, D., Chu, P.-H., Evans, S., &
1086 Chen, J. (2003). Embryonic atrial function is essential for mouse embryogenesis,
1087 cardiac morphogenesis and angiogenesis. Development (Cambridge, England),
1088 *130*(24), 6111–6119. https://doi.org/10.1242/dev.00831

1089 Hübner, K., Cabochette, P., Diéguez-Hurtado, R., Wiesner, C., Wakayama, Y.,
1090 Grassme, K. S., Hubert, M., Guenther, S., Belting, H.-G., Affolter, M., et al. (2018).
1091 Wnt/β-catenin signaling regulates VE-cadherin-mediated anastomosis of brain
1092 capillaries by counteracting S1pr1 signaling. Nature Communications, *9*(1), 4860.
1093 https://doi.org/10.1038/s41467-018-07302-x

1094 Huveneers, S., Oldenburg, J., Spanjaard, E., van der Krogt, G., Grigoriev, I.,
1095 Akhmanova, A., Rehmann, H., & de Rooij, J. (2012). Vinculin associates with
1096 endothelial VE-cadherin junctions to control force-dependent remodeling. The
1097 Journal of Cell Biology, *196*(5), 641–652. https://doi.org/10.1083/jcb.201108120

1098 Juettner, V. V, Kruse, K., Dan, A., Vu, V. H., Khan, Y., Le, J., Leckband, D., Komarova,
1099 Y., & Malik, A. B. (2019). VE-PTP stabilizes VE-cadherin junctions and the
1100 endothelial barrier via a phosphatase-independent mechanism. The Journal of Cell
1101 Biology, *218*(5), 1725–1742. https://doi.org/10.1083/jcb.201807210

1102 Ketema, M., Wilhelmsen, K., Kuikman, I., Janssen, H., Hodzic, D., & Sonnenberg, A.
1103 (2007). Requirements for the localization of nesprin-3 at the nuclear envelope and
1104 its interaction with plectin. Journal of Cell Science, *120*(Pt 19), 3384–3394.
1105 https://doi.org/10.1242/jcs.014191

1106 King, S. J., Nowak, K., Suryavanshi, N., Holt, I., Shanahan, C. M., & Ridley, A. J.
1107 (2014). Nesprin-1 and nesprin-2 regulate endothelial cell shape and migration.
1108 Cytoskeleton (Hoboken, N.J.), *71*(7), 423–434. https://doi.org/10.1002/cm.21182

1109 Komarova, Y. A., Huang, F., Geyer, M., Daneshjou, N., Garcia, A., Idalino, L., Kreutz,
1110 B., Mehta, D., & Malik, A. B. (2012). VE-cadherin signaling induces EB3
1111 phosphorylation to suppress microtubule growth and assemble adherens junctions.
1112 Molecular Cell, *48*(6), 914–925.

1113 Komarova, Y., Lansbergen, G., Galjart, N., Grosveld, F., Borisy, G. G., & Akhmanova,
1114 A. (2005). EB1 and EB3 control CLIP dissociation from the ends of growing
1115 microtubules. Molecular Biology of the Cell, *16*(11), 5334–5345.
1116 https://doi.org/10.1091/mbc.e05-07-0614

1117 Krendel, M., Zenke, F. T., & Bokoch, G. M. (2002). Nucleotide exchange factor GEF-H1
1118 mediates cross-talk between microtubules and the actin cytoskeleton. Nature Cell
1119 Biology, *4*(4), 294–301. https://doi.org/10.1038/ncb773

1120 Kushner, E. J., & Bautch, V. L. (2013). Building blood vessels in development and
1121 disease. Current Opinion in Hematology, *20*(3), 231–236.
1122 https://doi.org/10.1097/MOH.0b013e328360614b

1123 Kushner, E. J., Ferro, L. S., Liu, J.-Y., Durrant, J. R., Rogers, S. L., Dudley, A. C., &
1124 Bautch, V. L. (2014). Excess centrosomes disrupt endothelial migration via
1125 centrosome scattering. Journal of Cell Biology, *206*(2), 257–272.

1126 Kushner, E. J., Ferro, L. S., Yu, Z., & Bautch, V. L. (2016). Excess centrosomes perturb
1127 dynamic endothelial cell repolarization during blood vessel formation. Molecular
1128 Biology of the Cell, *27*(12), 1911–1920.

1129 Lei, K., Zhang, X., Ding, X., Guo, X., Chen, M., Zhu, B., Xu, T., Zhuang, Y., Xu, R., &
1130 Han, M. (2009). SUN1 and SUN2 play critical but partially redundant roles in
1131 anchoring nuclei in skeletal muscle cells in mice. PNAS, *106*(25), 10207–10212.

1132 Li, P., Stumpf, M., Müller, R., Eichinger, L., Glöckner, G., & Noegel, A. A. (2017). The
1133 function of the inner nuclear envelope protein SUN1 in mRNA export is regulated
1134 by phosphorylation. Scientific Reports, *7*(1), 9157. https://doi.org/10.1038/s41598-
1135 017-08837-7

1136 Ligon, L. A., Karki, S., Tokito, M., & Al, E. (2001). Dynein binds to beta-catenin and may
1137 tether microtubules at adherens junctions. Nature Cell Biology, *3*, 913–917.

1138 Linkert, M., Rueden, C. T., Allan, C., Burel, J.-M., Moore, W., Patterson, A., Loranger,
1139 B., Moore, J., Neves, C., MacDonald, D., et al. (2010). Metadata matters: access to
1140 image data in the real world. Journal of Cell Biology, *189*(5), 777–782.
1141 https://doi.org/10.1083/jcb.201004104

1142 Liu, Z., Ruter, D. L., Quigley, K., Tanke, N. T., Jiang, Y., & Bautch, V. L. (2021). Single-
1143 Cell RNA Sequencing Reveals Endothelial Cell Transcriptome Heterogeneity Under
1144 Homeostatic Laminar Flow. Arteriosclerosis, Thrombosis, and Vascular Biology,
1145 *41*(10), 2575–2584. https://doi.org/10.1161/ATVBAHA.121.316797

1146 Love, M. I., Huber, W., & Anders, S. (2014). Moderated estimation of fold change and
1147 dispersion for RNA-seq data with DESeq2. Genome Biology, *15*(12), 550.
1148 https://doi.org/10.1186/s13059-014-0550-8

1149 Maurya, M. R., Gupta, S., Li, J. Y.-S., Ajami, N. E., Chen, Z. B., Shyy, J. Y.-J., Chien,
1150 S., & Subramaniam, S. (2021). Longitudinal shear stress response in human
1151 endothelial cells to atheroprone and atheroprotective conditions. Proceedings of the
1152 National Academy of Sciences of the United States of America, *118*(4).
1153 https://doi.org/10.1073/pnas.2023236118

1154 Mavria, G., Vercoulen, Y., Yeo, M., Paterson, H., Karasarides, M., Marais, R., Bird, D.,
1155 & Marshall, C. J. (2006). ERK-MAPK signaling opposes Rho-kinase to promote

1156 endothelial cell survival and sprouting during angiogenesis. Cancer Cell, *9*(1), 33–
1157 44. https://doi.org/10.1016/j.ccr.2005.12.021

1158 May, C. K., & Carroll, C. W. (2018). Differential incorporation of SUN-domain proteins
1159 into LINC complexes is coupled to gene expression. PloS One, *13*(5), e0197621.
1160 https://doi.org/10.1371/journal.pone.0197621

1161 McGee, M. D., Rillo, R., Anderson, A. S., & Starr, D. A. (2006). UNC-83 IS a KASH
1162 protein required for nuclear migration and is recruited to the outer nuclear
1163 membrane by a physical interaction with the SUN protein UNC-84. Molecular
1164 Biology of the Cell, *17*(4), 1790–1801. https://doi.org/10.1091/mbc.e05-09-0894

1165 Meng, W., Mushika, Y., Ichii, T., & Takeichi, M. (2008). Anchorage of microtubule minus
1166 ends to adherens junctions regulates epithelial cell-cell contacts. Cell, *135*(5), 948–
1167 959. https://doi.org/10.1016/j.cell.2008.09.040

1168 Meyerzon, M., Fridolfsson, H. N., Ly, N., McNally, F. J., & Starr, D. A. (2009). UNC-83 is
1169 a nuclear-specific cargo adaptor for kinesin-1-mediated nuclear migration.
1170 Development (Cambridge, England), *136*(16), 2725–2733.
1171 https://doi.org/10.1242/dev.038596

1172 Montero-Balaguer, M., Swirsding, K., Orsenigo, F., Cotelli, F., Mione, M., & Dejana, E.
1173 (2009). Stable vascular connections and remodeling require full expression of VE-
1174 cadherin in zebrafish embryos. PloS One, *4*(6), e5772.
1175 https://doi.org/10.1371/journal.pone.0005772

1176 Morgan, J. T., Pfeiffer, E. R., Thirkill, T. L., Kumar, P., Peng, G., Fridolfsson, H. N.,
1177 Douglas, G. C., Starr, D. A., & Barakat, A. I. (2011). Nesprin-3 regulates endothelial
1178 cell morphology, perinuclear cytoskeletal architecture, and flow-induced
1179 polarization. Molecular Biology of the Cell, *22*(22), 4324–4334.
1180 https://doi.org/10.1091/mbc.E11-04-0287

1181 Nakatsu, M. N., & Hughes, C. C. W. (2008). An optimized three-dimensional in vitro
1182 model for the analysis of angiogenesis. Methods in Enzymology, *443*, 65–82.

1183 Nesmith, J. E., Chappell, J. C., Cluceru, J. G., & Bautch, V. L. (2017). Blood vessel
1184 anastomosis is spatially regulated by Flt1 during angiogenesis. Development
1185 (Cambridge, England), *144*(5), 889–896. https://doi.org/10.1242/dev.145672

1186 Neto, F., Klaus-Bergmann, A., Ong, Y. T., Alt, S., Vion, A.-C., Szymborska, A.,
1187 Carvalho, J. R., Hollfinger, I., Bartels-Klein, E., Franco, C. A., et al. (2018). YAP
1188 and TAZ regulate adherens junction dynamics and endothelial cell distribution
1189 during vascular development. ELife, *7*. https://doi.org/10.7554/eLife.31037

1190 Olive, M., Harten, I., Mitchell, R., Beers, J. K., Djabali, K., Cao, K., Erdos, M. R., Blair,
1191 C., Funke, B., Smoot, L., et al. (2010). Cardiovascular pathology in Hutchinson-
1192 Gilford progeria: correlation with the vascular pathology of aging. Arteriosclerosis,
1193 Thrombosis, and Vascular Biology, *30*(11), 2301–2309.
1194 https://doi.org/10.1161/ATVBAHA.110.209460

1195 Osmanagic-Myers, S., Kiss, A., Manakanatas, C., Hamza, O., Sedlmayer, F., Szabo, P.
1196 L., Fischer, I., Fichtinger, P., Podesser, B. K., Eriksson, M., et al. (2019).
1197 Endothelial progerin expression causes cardiovascular pathology through an
1198 impaired mechanoresponse. The Journal of Clinical Investigation, *129*(2), 531–545.
1199 https://doi.org/10.1172/JCI121297

1200 Ostlund, C., Folker, E. S., Choi, J. C., Gomes, E. R., Gundersen, G. G., & Worman, H.
1201 J. (2009). Dynamics and molecular interactions of linker of nucleoskeleton and
1202 cytoskeleton (LINC) complex proteins. Journal of Cell Science, *122*(Pt 22), 4099–
1203 4108. https://doi.org/10.1242/jcs.057075

1204 Padmakumar, V. C., Libotte, T., Lu, W., Zaim, H., Abraham, S., Noegel, A. A.,
1205 Gotzmann, J., Foisner, R., & Karakesisoglou, I. (2005). The inner nuclear
1206 membrane protein Sun1 mediates the anchorage of Nesprin-2 to the nuclear
1207 envelope. Journal of Cell Science, *118*(Pt 15), 3419–3430.
1208 https://doi.org/10.1242/jcs.02471

1209 Putri, G. H., Anders, S., Pyl, P. T., Pimanda, J. E., & Zanini, F. (2022). Analysing high-
1210 throughput sequencing data in Python with HTSeq 2.0. Bioinformatics (Oxford,
1211 England). https://doi.org/10.1093/bioinformatics/btac166

1212 Rauzi, M., Lenne, P.-F., & Lecuit, T. (2010). Planar polarized actomyosin contractile
1213 flows control epithelial junction remodelling. Nature, *468*(7327), 1110–1114.
1214 https://doi.org/10.1038/nature09566

1215 Rho, S.-S., Ando, K., & Fukuhara, S. (2017). Dynamic Regulation of Vascular
1216 Permeability by Vascular Endothelial Cadherin-Mediated Endothelial Cell-Cell
1217 Junctions. Journal of Nippon Medical School = Nippon Ika Daigaku Zasshi, *84*(4),
1218 148–159. https://doi.org/10.1272/jnms.84.148

1219 Ricard, N., Ciais, D., Levet, S., Subileau, M., Mallet, C., Zimmers, T. A., Lee, S.-J.,
1220 Bidart, M., Feige, J.-J., & Bailly, S. (2012). BMP9 and BMP10 are critical for
1221 postnatal retinal vascular remodeling. Blood, *119*(25), 6162–6171.
1222 https://doi.org/10.1182/blood-2012-01-407593

1223 Ruter, D. L., Liu, Z., Ngo, K. M., X, S., Marvin, A., Buglak, D. B., Kidder, E. J., & Bautch,
1224 V. L. (2021). SMAD6 transduces endothelial cell flow responses required for blood
1225 vessel homeostasis. Angiogenesis, *24*(2), 387–398.
1226 https://doi.org/10.1007/s10456-021-09777-7

1227 Sauteur, L., Affolter, M., & Belting, H.-G. (2017). Distinct and redundant functions of
1228 Esam and VE-cadherin during vascular morphogenesis. Development.
1229 https://doi.org/10.1242/dev.140038

1230 Sauteur, L., Krudewig, A., Herwig, L., Ehrenfeuchter, N., Lenard, A., Affolter, M., &
1231 Belting, H.-G. (2014). Cdh5/VE-cadherin Promotes Endothelial Cell Interface
1232 Elongation via Cortical Actin Polymerization during Angiogenic Sprouting. Cell
1233 Reports, *9*(2), 504–513. https://doi.org/10.1016/j.celrep.2014.09.024

1234 Schindelin, J., Arganda-Carreras, I., Frise, E., Kaynig, V., Longair, M., Pietzsch, T.,

1235 Preibisch, S., Rueden, C., Saalfeld, S., Schmid, B., et al. (2012). Fiji: an open-
1236 source platform for biological-image analysis. Nature Methods, *9*(7), 676–682.
1237 https://doi.org/10.1038/nmeth.2019

1238 Seebach, J., Dieterich, P., Luo, F., Schillers, H., Vestweber, D., Oberleithner, H., Galla,
1239 H. J., & Schnittler, H. J. (2000). Endothelial barrier function under laminar fluid
1240 shear stress. Laboratory Investigation; a Journal of Technical Methods and
1241 Pathology, *80*(12), 1819–1831. https://doi.org/10.1038/labinvest.3780193

1242 Sehrawat, S., Cullere, X., Patel, S., Italiano, J., & Mayadas, T. N. (2008). Role of Epac1,
1243 an exchange factor for Rap GTPases, in endothelial microtubule dynamics and
1244 barrier function. Molecular Biology of the Cell, *19*(3), 1261–1270.
1245 https://doi.org/10.1091/mbc.e06-10-0972

1246 Sehrawat, S., Ernandez, T., Cullere, X., Takahashi, M., Ono, Y., Komarova, Y., &
1247 Mayadas, T. N. (2011). AKAP9 regulation of microtubule dynamics promotes
1248 Epac1-induced endothelial barrier properties. Blood, *117*(2), 708–718.
1249 https://doi.org/10.1182/blood-2010-02-268870

1250 Shaw, R. M., Fay, A. J., Puthenveedu, M. A., von Zastrow, M., Jan, Y.-N., & Jan, L. Y.
1251 (2007). Microtubule plus-end-tracking proteins target gap junctions directly from the
1252 cell interior to adherens junctions. Cell, *128*(3), 547–560.
1253 https://doi.org/10.1016/j.cell.2006.12.037

1254 Sörensen, I., Adams, R. H., & Gossler, A. (2009). DLL1-mediated Notch activation
1255 regulates endothelial identity in mouse fetal arteries. Blood, *113*(22), 5680–5688.
1256 https://doi.org/10.1182/blood-2008-08-174508

1257 Starr, D. A., & Fridolfsson, H. N. (2010). Interactions between nuclei and the
1258 cytoskeleton are mediated by SUN-KASH nuclear-envelope bridges. Annual
1259 Review of Cell and Developmental Biology, *26*, 421–444.
1260 https://doi.org/10.1146/annurev-cellbio-100109-104037

1261 Stehbens, S. J., Paterson, A. D., Crampton, M. S., Shewan, A. M., Ferguson, C.,
1262 Akhmanova, A., Parton, R. G., & Yap, A. S. (2006). Dynamic microtubules regulate
1263 the local concentration of E-cadherin at cell-cell contacts. Journal of Cell Science,
1264 *119*(Pt 9), 1801–1811. https://doi.org/10.1242/jcs.02903

1265 Stewart-Hutchinson, P. J., Hale, C. M., Wirtz, D., & Hodzic, D. (2008). Structural
1266 requirements for the assembly of LINC complexes and their function in cellular
1267 mechanical stiffness. Experimental Cell Research, *314*(8), 1892–1905.
1268 https://doi.org/10.1016/j.yexcr.2008.02.022

1269 Stewart, R. M., Zubek, A. E., Rosowski, K. A., Schreiner, S. M., Horsley, V., & King, M.
1270 C. (2015). Nuclear-cytoskeletal linkages facilitate cross talk between the nucleus
1271 and intercellular adhesions. The Journal of Cell Biology, *209*(3), 403–418.
1272 https://doi.org/10.1083/jcb.201502024

1273 Stroud, M. J., Feng, W., Zhang, J., Veevers, J., Fang, X., Gerace, L., & Chen, J. (2017).
1274 Nesprin 1α2 is essential for mouse postnatal viability and nuclear positioning in

1275 skeletal muscle. The Journal of Cell Biology, *216*(7), 1915–1924.
1276 https://doi.org/10.1083/jcb.201612128

1277 Szymborska, A., & Gerhardt, H. (2018). Hold Me, but Not Too Tight-Endothelial Cell-
1278 Cell Junctions in Angiogenesis. Cold Spring Harbor Perspectives in Biology, *10*(8).
1279 https://doi.org/10.1101/cshperspect.a029223

1280 Taranum, S., Sur, I., Müller, R., Lu, W., Rashmi, R. N., Munck, M., Neumann, S.,
1281 Karakesisoglou, I., & Noegel, A. A. (2012). Cytoskeletal interactions at the nuclear
1282 envelope mediated by nesprins. International Journal of Cell Biology, *2012*,
1283 736524. https://doi.org/10.1155/2012/736524

1284 Thakar, K., May, C. K., Rogers, A., & Carroll, C. W. (2017). Opposing roles for distinct
1285 LINC complexes in regulation of the small GTPase RhoA. Molecular Biology of the
1286 Cell, *28*(1), 182–191. https://doi.org/10.1091/mbc.E16-06-0467

1287 Tkachenko, E., Gutierrez, E., Saikin, S. K., Fogelstrand, P., Kim, C., Groisman, A., &
1288 Ginsberg, M. H. (2013). The nucleus of endothelial cell as a sensor of blood flow
1289 direction. Biology Open, *2*(10), 1007–1012. https://doi.org/10.1242/bio.20134622

1290 Ueda, N., Maekawa, M., Matsui, T. S., Deguchi, S., Takata, T., Katahira, J.,
1291 Higashiyama, S., & Hieda, M. (2022). Inner Nuclear Membrane Protein, SUN1, is
1292 Required for Cytoskeletal Force Generation and Focal Adhesion Maturation.
1293 Frontiers in Cell and Developmental Biology, *10*, 885859.
1294 https://doi.org/10.3389/fcell.2022.885859

1295 van Ingen, M. J. A., & Kirby, T. J. (2021). LINCing Nuclear Mechanobiology With
1296 Skeletal Muscle Mass and Function. Frontiers in Cell and Developmental Biology,
1297 *9*, 690577. https://doi.org/10.3389/fcell.2021.690577

1298 Vasileva, E., & Citi, S. (2018). The role of microtubules in the regulation of epithelial
1299 junctions. Tissue Barriers, *6*(3), 1539596.
1300 https://doi.org/10.1080/21688370.2018.1539596

1301 Verin, A. D., Birukova, A., Wang, P., Liu, F., Becker, P., Birukov, K., & Garcia, J. G.
1302 (2001). Microtubule disassembly increases endothelial cell barrier dysfunction: role
1303 of MLC phosphorylation. American Journal of Physiology. Lung Cellular and
1304 Molecular Physiology, *281*(3), L565-74.
1305 https://doi.org/10.1152/ajplung.2001.281.3.L565

1306 Vion, A.-C., Perovic, T., Petit, C., Hollfinger, I., Bartels-Klein, E., Frampton, E., Gordon,
1307 E., Claesson-Welsh, L., & Gerhardt, H. (2020). Endothelial Cell Orientation and
1308 Polarity Are Controlled by Shear Stress and VEGF Through Distinct Signaling
1309 Pathways. Frontiers in Physiology, *11*, 623769.
1310 https://doi.org/10.3389/fphys.2020.623769

1311 Wacker, A., & Gerhardt, H. (2011). Endothelial development taking shape. Current
1312 Opinion in Cell Biology, *23*(6), 676–685. https://doi.org/10.1016/j.ceb.2011.10.002

1313 Wimmer, R., Cseh, B., Maier, B., Scherrer, K., & Baccarini, M. (2012). Angiogenic

1314 sprouting requires the fine tuning of endothelial cell cohesion by the Raf-1/Rok-α
1315 complex. Developmental Cell, *22*(1), 158–171.
1316 https://doi.org/10.1016/j.devcel.2011.11.012

1317 Wright, C. E., Kushner, E. J., Du, Q., & Bautch, V. L. (2015). LGN directs interphase
1318 endothelial cell behavior via the microtubule network. PLoS ONE, *10*(9), 1–15.
1319 https://doi.org/10.1371/journal.pone.0138763

1320 Wylie, L. A., Mouillesseaux, K. P., Chong, D. C., & Bautch, V. L. (2018). Developmental
1321 SMAD6 loss leads to blood vessel hemorrhage and disrupted endothelial cell
1322 junctions. Developmental Biology, *442*(2), 199–209.
1323 https://doi.org/10.1016/j.ydbio.2018.07.027

1324 Yang, F., Zhang, Y., Zhu, J., Wang, J., Jiang, Z., Zhao, C., Yang, Q., Huang, Y., Yao,
1325 W., Pang, W., et al. (2020). Laminar Flow Protects Vascular Endothelial Tight
1326 Junctions and Barrier Function via Maintaining the Expression of Long Non-coding
1327 RNA MALAT1. Frontiers in Bioengineering and Biotechnology, *8*, 647.
1328 https://doi.org/10.3389/fbioe.2020.00647

1329 Zhang, J., Felder, A., Liu, Y., Guo, L. T., Lange, S., Dalton, N. D., Gu, Y., Peterson, K.
1330 L., Mizisin, A. P., Shelton, G. D., et al. (2010). Nesprin 1 is critical for nuclear
1331 positioning and anchorage. Human Molecular Genetics, *19*(2), 329–341.
1332 https://doi.org/10.1093/hmg/ddp499

1333 Zhang, Q., Ragnauth, C. D., Skepper, J. N., Worth, N. F., Warren, D. T., Roberts, R. G.,
1334 Weissberg, P. L., Ellis, J. A., & Shanahan, C. M. (2005). Nesprin-2 is a multi-
1335 isomeric protein that binds lamin and emerin at the nuclear envelope and forms a
1336 subcellular network in skeletal muscle. Journal of Cell Science, *118*(Pt 4), 673–687.
1337 https://doi.org/10.1242/jcs.01642

1338 Zhang, X., Lei, K., Yuan, X., Wu, X., Zhuang, Y., Xu, T., Xu, R., & Han, M. (2009).
1339 SUN1/2 and Syne/Nesprin-1/2 complexes connect centrosome to the nucleus
1340 during neurogenesis and neuronal migration in mice. Neuron, *64*(2), 173–187.
1341 https://doi.org/10.1016/j.neuron.2009.08.018

1342 Zhou, C., Li, C., Zhou, B., Sun, H., Koullourou, V., Holt, I., Puckelwartz, M. J., Warren,
1343 D. T., Hayward, R., Lin, Z., et al. (2017). Novel nesprin-1 mutations associated with
1344 dilated cardiomyopathy cause nuclear envelope disruption and defects in
1345 myogenesis. Human Molecular Genetics, *26*(12), 2258–2276.
1346 https://doi.org/10.1093/hmg/ddx116

1347 Zhu, R., Antoku, S., & Gundersen, G. G. (2017). Centrifugal Displacement of Nuclei
1348 Reveals Multiple LINC Complex Mechanisms for Homeostatic Nuclear Positioning.
1349 Current Biology : CB, *27*(20), 3097-3110.e5.
1350 https://doi.org/10.1016/j.cub.2017.08.073

1351

1352 **FIGURE LEGENDS**

1353 **Figure 1. The nuclear LINC protein SUN1 regulates vascular development.**

1354 **(a)** Schematic of tamoxifen-induced excision of exon 4 of *Sun1* in pups from cross of
1355 *Sun1*$^{fl/fl}$ X *Sun1*$^{fl/+}$*;Cdh5CreERT2* mice. **(b)** Representative images of P7 mouse retinas
1356 of indicated genotypes, stained for IB4 (isolectin). Scale bar, 500μm. Inset shows
1357 vascular plexus ahead of vein. Red line shows expansion of vascular front. Scale bar
1358 inset, 150μm. **(c)** Quantification of vessel network radial expansion in **b**. n=186 ROIs
1359 from 44 retinas (controls) and 63 ROIs from 16 retinas (*Sun1*^{iECKO}) from 6 independent
1360 litters. ****, p<0.0001 by student's two-tailed unpaired *t*-test. **(d)** Quantification of
1361 vascular density ahead of either arteries or veins. n=87 ROIs (controls, artery), 38 ROIs
1362 (*Sun1*^{iECKO}, artery), 84 ROIs (controls, vein), and 37 ROIs (*Sun1*^{iECKO}, vein) from 27
1363 retinas (controls) and 12 retinas (*Sun1*^{iECKO}) from 3 independent litters. **, p<0.01 by
1364 student's two-tailed unpaired *t*-test. **(e)** Representative images of IB4 (isolectin) (green,
1365 vessels) and VE-cadherin (white, junctions) staining in P7 retinas of indicated
1366 genotypes. Scale bar, 50μm. **(f)** Quantification of ectopic VE-cadherin as shown in **e**.
1367 n=144 junctions (9 retinas, controls) and 160 junctions (10 retinas, *Sun1*^{iECKO}). ****,
1368 p<0.0001 by student's two-tailed unpaired *t*-test.

1369

1370 **Figure 2. Nuclear SUN1 is required for sprouting angiogenesis.**

1371 **(a)** Representative images of HUVEC with indicated siRNAs in 3D angiogenic sprouting
1372 assay. Sprouts were stained for Phalloidin (actin) and then depth encoded such that
1373 cooler colors are further in the Z-plane and warmer colors are closer in the Z-plane.
1374 Scale bar, 100μm. **(b)** Quantification of average sprout length of 3D angiogenic sprouts
1375 shown in **a**. n=42 beads (NT) and 43 beads (SUN1 KD) compiled from 5 replicates. ****,
1376 p<0.0001 by student's two-tailed unpaired *t*-test. **(c)** Quantification of branches/mm of

1377 3D angiogenic sprouts shown in **a**. n=41 beads (NT) and 43 beads (SUN1 KD) compiled
1378 from 5 replicates. ****, $p<0.0001$ by student's two-tailed unpaired *t*-test. **(d)** Stills from
1379 Movie S1 and Movie S2 showing sprouting dynamics of HUVEC with indicated siRNAs
1380 over 50h. Scale bar, 50μm. **(e)** Quantification of HUVEC sprout extensions and
1381 retractions shown in **d**. n=101 sprouts (NT) and 77 sprouts (SUN1 KD) compiled from 3
1382 replicates. $p<0.001$ by χ^2 analysis. **(f)** Representative images of HUVEC with indicated
1383 siRNAs and stained with indicated antibodies in the 3D sprouting angiogenesis assay.
1384 Endothelial cells were stained for DAPI (cyan, DNA), phalloidin (green, actin), and VE-
1385 cadherin (white, junctions). Arrows indicate normal junctions; arrowheads indicate
1386 abnormal junctions. Scale bar, 20μm. **(g)** Quantification of ectopic VE-cadherin as
1387 shown in **f**. n=32 junctions (NT) and 30 junctions (SUN1 KD) compiled from 2 replicates.
1388 ****, $p<0.0001$ by student's two-tailed unpaired *t*-test.
1389

1390 **Figure 3. SUN1 regulates actin dynamics and angiogenic sprout extension *in***
1391 ***vivo*.**
1392 **(a)** Representative images of zebrafish embryos at 34 hpf with indicated morpholino
1393 treatments; anterior to left. *Tg(fli:LifeAct-GFP)* (green, vessels). Insets show ISVs with
1394 filopodia, outlines highlighted to show filopodia. Scale bar, 20μm. **(b)** Quantification of
1395 filopodia number shown in **a**. n=39 ROIs (15 fish, NT) and 56 ROIs (20 fish, *sun1b* MO)
1396 compiled from 3 replicates. **, $p<0.01$ by student's two-tailed unpaired *t*-test. **(c)**
1397 Quantification of average filopodia length shown in **a**. n=39 ROIs (15 fish, NT MO) and
1398 56 ROIs (20 fish, *sun1b* MO) compiled from 3 replicates. ****, $p<0.0001$ by student's
1399 two-tailed unpaired *t*-test. **(d)** Representative images of zebrafish embryos at 34 hpf
1400 with indicated genotypes; anterior to left. *Tg(fli:LifeAct-GFP)* (green, vessels). Insets
1401 show ISVs with filopodia, outlines highlighted to show filopodia. Scale bar, 20μm. **(e)**

1402 Quantification of filopodia number shown in **d**. n=27 ROIs (9 fish, *sun1b*$^{+/+}$) and 30 ROIs
1403 (10 fish, *sun1b* ^{sa33109}) compiled from 2 replicates. ns, not significant by student's two-
1404 tailed unpaired *t*-test. **(f)** Quantification of average filopodia length shown in **d**. n=27
1405 ROIs (9 fish, *sun1b* $^{+/+}$) and 30 ROIs (10 fish, *sun1b* ^{sa33109}) compiled from 2 replicates.
1406 **, p<0.01 by student's two-tailed unpaired *t*-test. **(g)** Stills from Movie S3 and Movie S4
1407 showing ISV sprouting from 26 hpf to 36 hpf in zebrafish embryos with indicated
1408 morpholino treatment; anterior to left. *Tg(fli:LifeAct-GFP)* (green, vessels). White
1409 arrowhead points to ISV that does not extend or connect to DLAV. Yellow arrow points
1410 to ISV that extends but does not connect to DLAV. Scale bar, 20μm. **(h)** Quantification
1411 of ISV connection to DLAV shown in **g**. n=32 ISVs (6 fish, NT MO) and 36 ISVs (6 fish,
1412 *sun1b* MO) compiled from 2 replicates. p<0.05 by χ^2 analysis. **(i)** Representative images
1413 of zebrafish embryos at 34 hpf with indicated morpholino treatments; anterior to left.
1414 *Tg(fli:LifeAct-GFP)* (green, vessels); ZO-1 (white junctions). Outlines highlighted to
1415 show junction shapes. Scale bar, 10μm. **(j)** Quantification of junction morphology shown
1416 in **i**. n=136 junctions (21 fish, NT MO) and 142 junctions (22 fish, *sun1b* MO). ***,
1417 p<0.001 by student's two-tailed unpaired *t*-test.
1418

1419 **Figure 4. SUN1 stabilizes endothelial cell-cell junctions and regulates barrier**
1420 **function.**

1421 **(a)** Representative images of HUVEC with indicated knockdowns in monolayers.
1422 Endothelial cells were stained for DAPI (cyan, DNA) and VE-cadherin (white, junctions).
1423 Insets show junctions. Scale bar, 10μm. **(b)** Representative graph of impedance
1424 measured by RTCA. **(c)** Quantification of % change in cell index for RTCA measured at
1425 5h. Normalized to NT cell index. n=5 replicates. *, p<0.05 by student's two-tailed
1426 unpaired *t*-test. **(d)** Representative images of HUVEC with indicated siRNAs plated on

1427 biotinylated fibronectin and exposed to 15 dyn/cm^2 shear stress for 72 h then treated
1428 with streptavidin. Endothelial cells were stained for DAPI (cyan, DNA), streptavidin
1429 (green), and VE-cadherin (white, junctions). Arrow indicates flow direction. Insets show
1430 junctions. Scale bar, 20μm. **(e)** Quantification of cell alignment shown in **d**. n=59 cells
1431 (NT) and 73 cells (SUN1 KD) compiled from 3 replicates. **(f)** Quantification of
1432 streptavidin area shown in **d**. n=15 ROIs (NT) and 15 ROIS (SUN1 KD) compiled from 3
1433 replicates. **(g)** Representative images of HUVEC with indicated siRNAs showing
1434 adherens following EDTA washout. Endothelial cells were stained for DAPI (cyan, DNA)
1435 and VE-cadherin (white, junctions). Insets show junctions. Scale bar, 20μm. **(h)**
1436 Quantification of VE-cadherin line scans at 20 min, 40 min, and 60 min post EDTA
1437 washout in **g**. 20 min: n=31 junctions (NT) and 23 junctions (SUN1 KD); 40 min: n=49
1438 junctions (NT) and 33 junctions (SUN1 KD); 60 min: n=33 junctions (NT) and 33
1439 junctions (SUN1 KD) compiled from 3 replicates. ns, not significant; ****, $p<0.0001$ by
1440 student's two-tailed unpaired *t*-test.
1441

1442 **Figure 5. SUN1 regulates microtubule localization and dynamics in endothelial**
1443 **cells.**

1444 **(a)** Representative images of HUVEC with indicated siRNAs and indicated treatments.
1445 Endothelial cells were stained for DAPI (cyan, DNA) and VE-cadherin (white, junctions).
1446 Insets show junctions. Scale bar, 20μm. **(b)** Quantification of VE-cadherin line scans for
1447 treatments shown in **a**. n=106 junctions (NT, vehicle), 101 junctions (NT, Nocodazole),
1448 105 junctions (SUN1 KD, vehicle), and 96 junctions (SUN1 KD, Nocodazole) compiled
1449 from 3 replicates. ns, not significant; ****, $p<0.0001$ by two-way ANOVA with Tukey's
1450 multiple comparisons test. **(c)** Representative images of HUVEC with indicated siRNAs.
1451 Endothelial cells were stained for α-tubulin (cyan, microtubules) and VE-cadherin (red,

1452 junctions). Red insets show α-tubulin at the MTOC (microtubule organizing center),
1453 yellow insets show α-tubulin contacts at junctions. Scale bar, 20μm. **(d)** Quantification of
1454 α-tubulin area at the MTOC shown in **c**. n=19 cells (NT) and 10 cells (SUN1 KD)
1455 compiled from 3 replicates. ns, not significant by student's two-tailed unpaired *t*-test. **(e)**
1456 Quantification of peripheral α-tubulin area shown in **c**. n=39 cells (NT) and 46 cells
1457 (SUN1 KD) compiled from 3 replicates. ****, $p<0.0001$ by student's two-tailed unpaired
1458 *t*-test. **(f)** Quantification of contacts between α-tubulin and VE-cadherin shown in **c**.
1459 n=75 junctions (NT) and 48 junctions (SUN1 KD) compiled from 3 replicates. ***,
1460 $p<0.001$ by student's two-tailed unpaired *t*-test. **(g)** Stills from Movie S5 and Movie S6
1461 showing microtubule growth in EB3-mCherry labeled HUVEC. White dot indicates start
1462 of track. Yellow line indicates growth, red line indicates shrinkage. Scale bar, 10μm. **(h)**
1463 Quantification of microtubule growth rate from EB3-mCherry microtubule tracking.
1464 N=120 microtubules (12 cells, NT) and 117 microtubules (12 cells, SUN1 KD) compiled
1465 from 2 replicates. ns, not significant by student's two-tailed unpaired *t*-test. **(i)**
1466 Quantification of microtubule shrink rate from EB3-mCherry microtubule tracking. n=120
1467 microtubules (12 cells, NT) and 117 microtubules (12 cells, SUN1 KD) compiled from 2
1468 replicates. **, $p<0.01$ by student's two-tailed unpaired *t*-test. **(j)** Quantification of
1469 catastrophe rate from EB3-mCherry microtubule tracking. n=120 microtubules (12 cells,
1470 NT) and 117 microtubules (12 cells, SUN1 KD) compiled from 2 replicates. ****,
1471 $p<0.0001$ by student's two-tailed unpaired *t*-test. **(k)** Quantification of percent of time
1472 spent shrinking from EB3-mCherry microtubule tracking. n=120 microtubules (12 cells,
1473 NT) and 117 microtubules (12 cells, SUN1 KD) compiled from 2 replicates. ****,
1474 $p<0.0001$ by student's two-tailed unpaired *t*-test.
1475

1476 **Figure 6. SUN1 regulates endothelial cell contractility and exerts its effects on**
1477 **junctions through the microtubule-associated GEF-H1.**
1478 **(a)** Representative images of HUVEC with indicated siRNAs and indicated treatments.
1479 Endothelial cells were stained for DAPI (cyan, DNA) and VE-cadherin (white, junctions).
1480 Insets show junctions. Scale bar, 20μm. **(b)** Quantification of VE-cadherin line scans for
1481 treatments shown in **a**. n=159 junctions (NT, vehicle), 154 junctions (NT, blebbistatin),
1482 151 junctions (SUN1 KD, vehicle), and 149 junctions (SUN1 KD, blebbistatin) compiled
1483 from 3 replicates. ns, not significant; ****, $p<0.0001$ by two-way ANOVA with Tukey's
1484 multiple comparisons test. **(c)** Representative images of HUVEC with indicated siRNAs
1485 and indicated treatments. Endothelial cells were stained for DAPI (cyan, DNA) and VE-
1486 cadherin (white, junctions). Insets show junctions. Scale bar, 20μm. **(d)** Quantification of
1487 VE-cadherin line scans for treatments shown in **c**. n=75 junctions (NT, vehicle), 70
1488 junctions (NT, thrombin), 71 junctions (SUN1 KD, vehicle), and 73 junctions (SUN1 KD,
1489 thrombin) compiled from 3 replicates. ns, not significant; ****, $p<0.0001$ by two-way
1490 ANOVA with Tukey's multiple comparisons test. **(e)** Representative images of HUVEC
1491 with indicated siRNAs. Endothelial cells were stained for DAPI (blue, DNA), α-tubulin
1492 (red, microtubules), and GEF-H1 (cyan). Insets show α-tubulin and GEF-H1
1493 colocalization. Scale bar, 20μm. **(f)** Quantification of free GEF-H1 normalized to α-
1494 tubulin associated GEF-H1 shown in **e**. n=30 cells (NT) and 30 cells (SUN1 KD)
1495 compiled from 3 replicates. **, $p<0.01$ by student's two-tailed unpaired *t*-test. **(g)**
1496 Representative images of HUVEC with indicated siRNAs and indicated treatments.
1497 Endothelial cells were stained for DAPI (cyan, DNA) and VE-cadherin (white, junctions).
1498 Insets show junctions. Scale bar, 20μm. **(h)** Quantification of VE-cadherin line scans
1499 from knockdowns shown in **g**. n=169 junctions (NT), 166 junctions (SUN1 KD), 170

1500 junctions (SUN1/GEF-H1 KD) compiled from 3 replicates. ns, not significant; ****,
1501 $p<0.0001$ by one-way ANOVA with Tukey's multiple comparisons test.
1502
1503 **Figure 7. SUN1 regulates endothelial cell junctions through nesprin-1.**
1504 **(a)** Representative images of HUVEC with indicated siRNAs cultured on biotinylated
1505 fibronectin and treated with streptavidin upon confluence. Endothelial cells were stained
1506 for DAPI (cyan, DNA), Streptavidin (green), and VE-cadherin (white, junctions). Insets
1507 show junctions. Scale bar, 20μm. **(b)** Quantification of streptavidin area shown in **a**. n=6
1508 ROIs (NT), 6 ROIs (SUN1 KD), and 6 ROIs (SUN1/Nesprin-1 KD) from 1 representative
1509 replicate. *, $p<0.05$; ****, $p<0.0001$ by one-way ANOVA with Tukey's multiple
1510 comparisons test. **(c)** Model describing proposed role of SUN1 in angiogenic sprouting
1511 and endothelial cell junction stabilization.

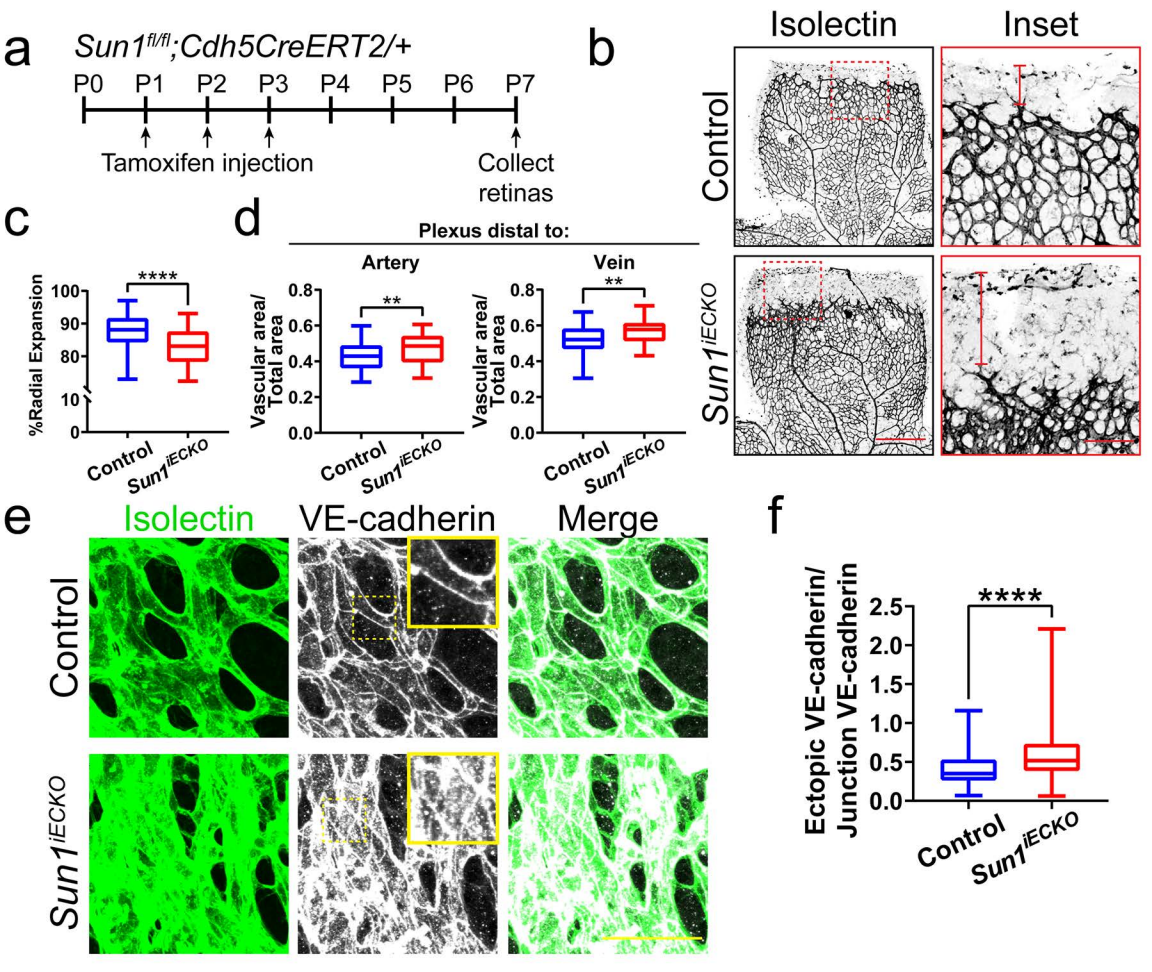
a
Sun1fl/fl;Cdh5CreERT2/+
P0
P1
P2
P3
P4
P5
P6
P7
Tamoxifen injection
Collect retinas
b
Isolectin
Inset
Control
Sun1iECKO
c
%Radial Expansion
****
Control
Sun1iECKO
d
Plexus distal to:
Artery
Vein
Vascular area/ Total area
**
**
Control
Sun1iECKO
e
Isolectin
VE-cadherin
Merge
Control
Sun1iECKO
f
Ectopic VE-cadherin/ Junction VE-cadherin
****
Control
Sun1iECKO

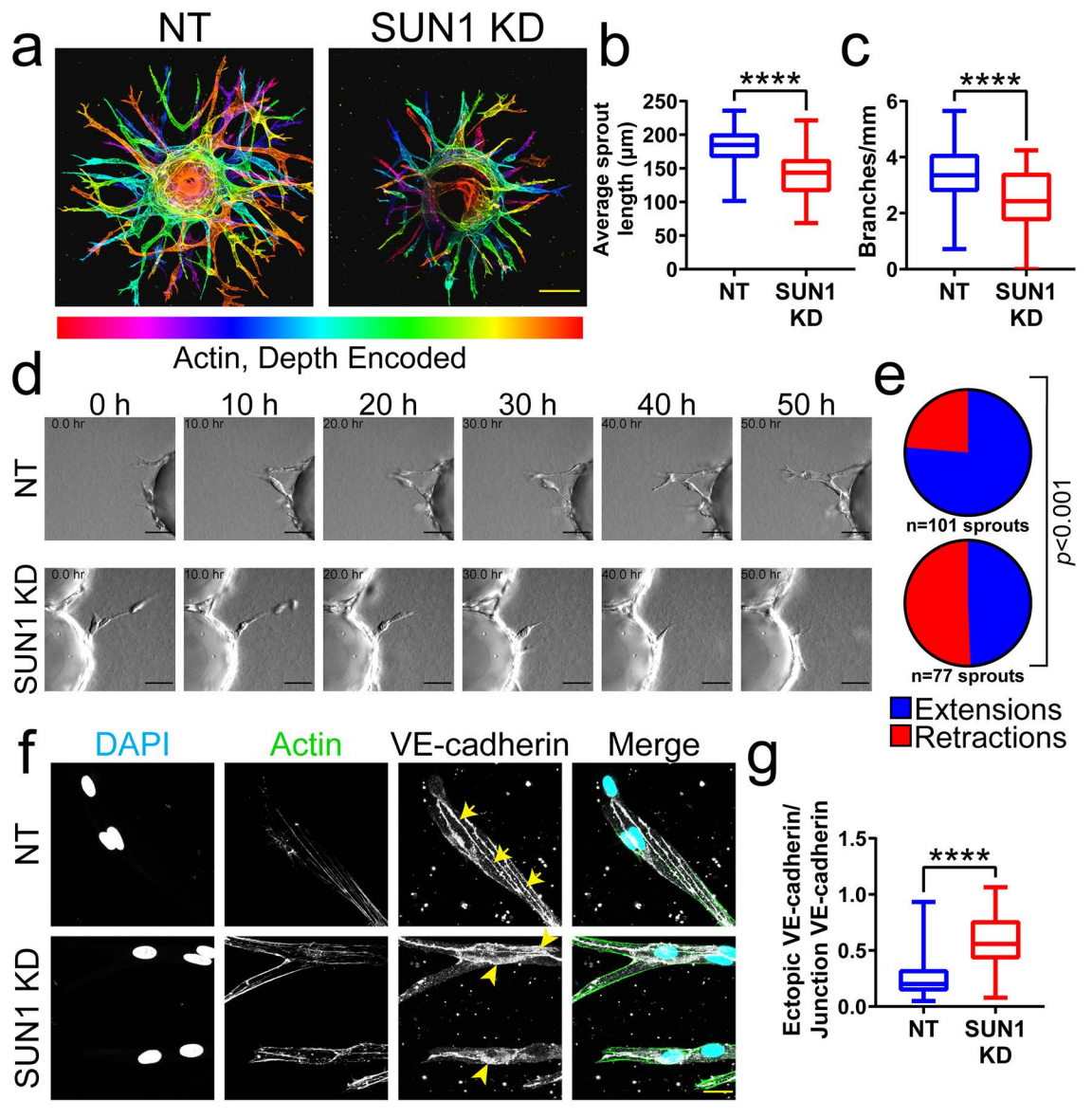
a
NT
SUN1 KD
Actin, Depth Encoded
b
****
Average sprout length (μm)
250
200
150
100
50
0
NT
SUN1 KD
c
****
Branches/mm
6
4
2
0
NT
SUN1 KD
d
0 h
10 h
20 h
30 h
40 h
50 h
NT
SUN1 KD
0.0 hr
10.0 hr
20.0 hr
30.0 hr
40.0 hr
50.0 hr
e
n=101 sprouts
n=77 sprouts
p<0.001
Extensions
Retractions
f
DAPI
Actin
VE-cadherin
Merge
NT
SUN1 KD
g
****
Ectopic VE-cadherin/ Junction VE-cadherin
1.5
1.0
0.5
0.0
NT
SUN1 KD

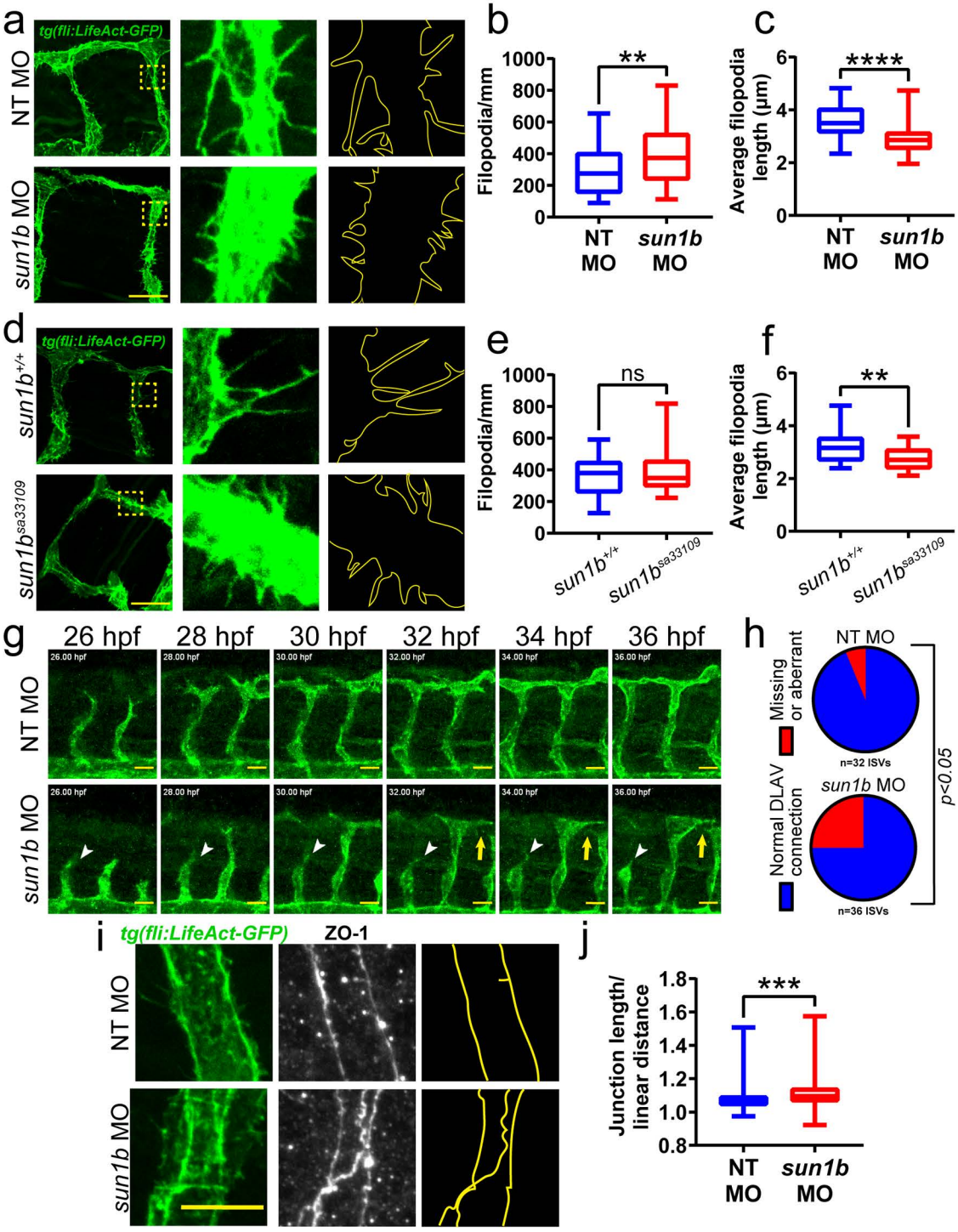
a
tg(fli:LifeAct-GFP)
NT MO
sun1b MO
b
Filopodia/mm
1000
800
600
400
200
0
**
NT MO
sun1b MO
c
Average filopodia length (µm)
6
4
2
0
****
NT MO
sun1b MO
d
tg(fli:LifeAct-GFP)
sun1b+/+
sun1bsa33109
e
Filopodia/mm
1000
800
600
400
200
0
ns
sun1b+/+
sun1bsa33109
f
Average filopodia length (µm)
6
4
2
0
**
sun1b+/+
sun1bsa33109
g
26 hpf
28 hpf
30 hpf
32 hpf
34 hpf
36 hpf
NT MO
sun1b MO
26.00 hpf
28.00 hpf
30.00 hpf
32.00 hpf
34.00 hpf
36.00 hpf
h
NT MO
Missing or aberrant
n=32 ISVs
sun1b MO
Normal DLAV connection
n=36 ISVs
p<0.05
i
tg(fli:LifeAct-GFP)
ZO-1
NT MO
sun1b MO
j
Junction length/ linear distance
1.8
1.6
1.4
1.2
1.0
0.8
***
NT MO
sun1b MO

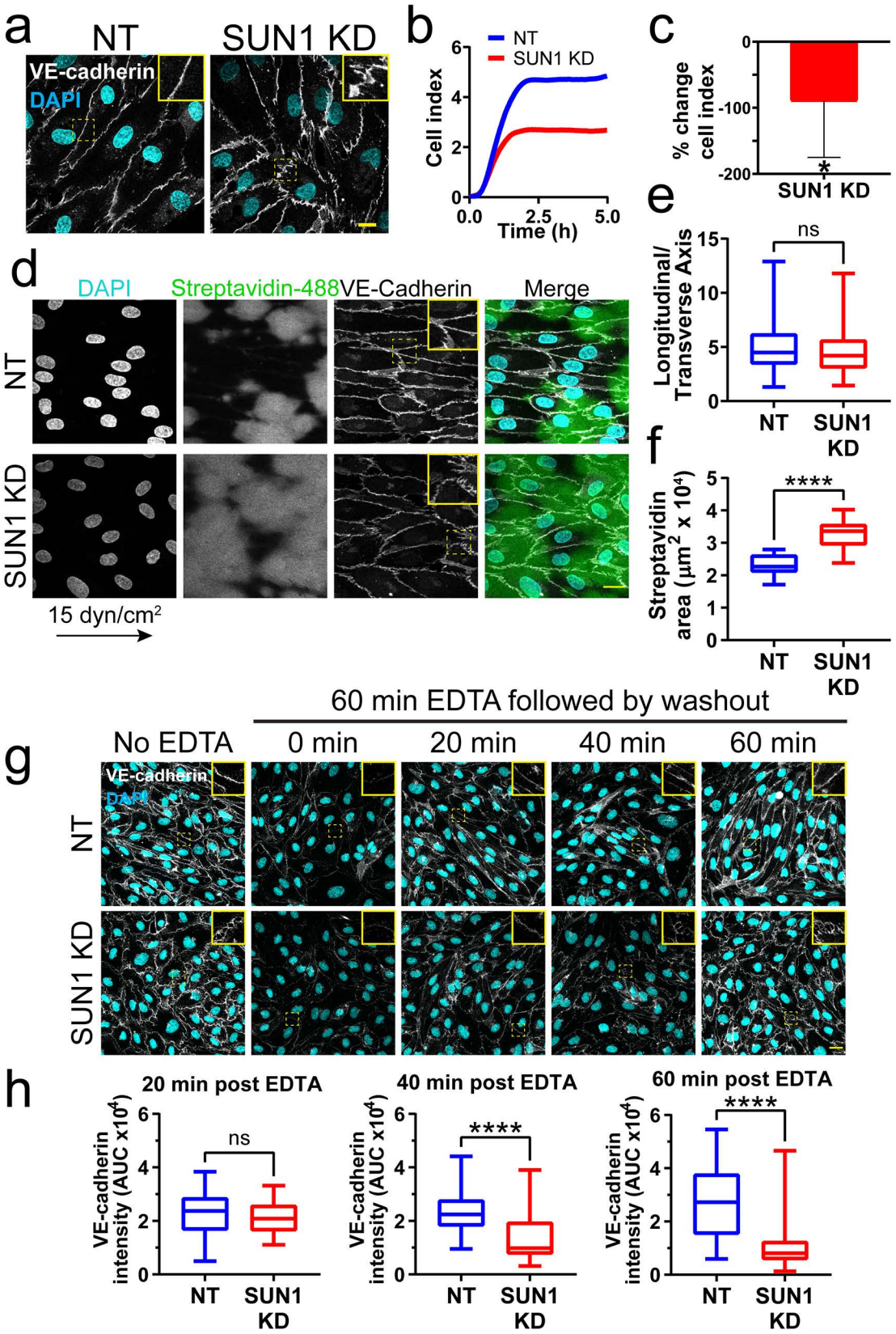
a
NT
SUN1 KD
VE-cadherin
DAPI
b
NT
SUN1 KD
Cell index
Time (h)
c
% change cell index
SUN1 KD
d
DAPI
Streptavidin-488
VE-Cadherin
Merge
NT
SUN1 KD
15 dyn/cm²
e
Longitudinal/ Transverse Axis
ns
NT
SUN1 KD
f
Streptavidin area (μm² x 10⁴)
****
NT
SUN1 KD
60 min EDTA followed by washout
No EDTA
0 min
20 min
40 min
60 min
g
VE-cadherin
DAPI
NT
SUN1 KD
h
20 min post EDTA
40 min post EDTA
60 min post EDTA
VE-cadherin intensity (AUC x10⁴)
ns
****
****
NT
SUN1 KD

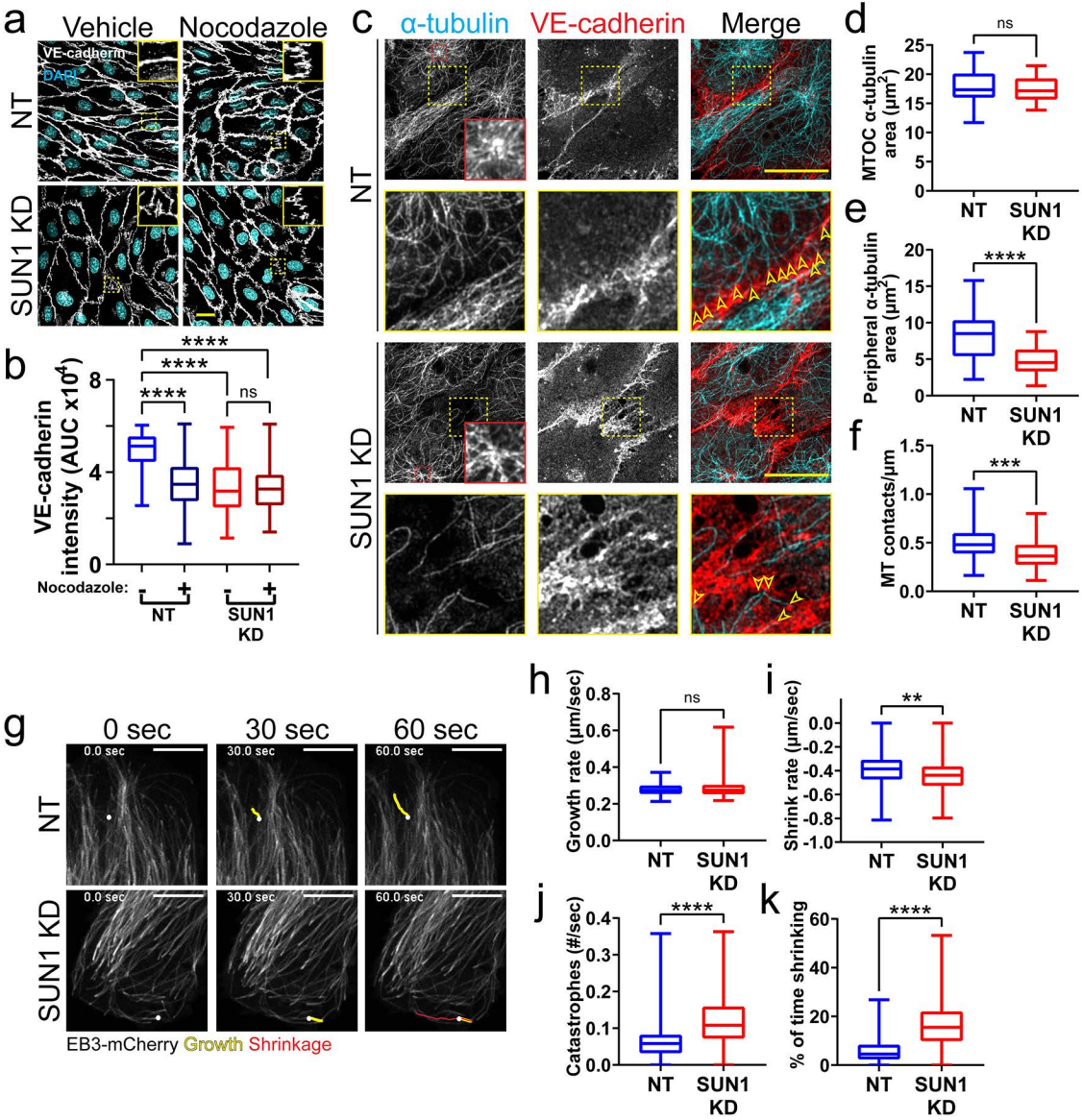
a
Vehicle
Nocodazole
VE-cadherin
DAPI
NT
SUN1 KD
b
VE-cadherin intensity (AUC x10^4)
****
****
****
ns
Nocodazole:
NT
SUN1 KD
c
α-tubulin
VE-cadherin
Merge
NT
SUN1 KD
d
MTOC α-tubulin area (μm²)
ns
e
Peripheral α-tubulin area (μm²)
****
f
MT contacts/μm
***
g
0 sec
30 sec
60 sec
NT
SUN1 KD
EB3-mCherry Growth Shrinkage
h
Growth rate (μm/sec)
ns
i
Shrink rate (μm/sec)
**
j
Catastrophes (#/sec)
****
k
% of time shrinking
****

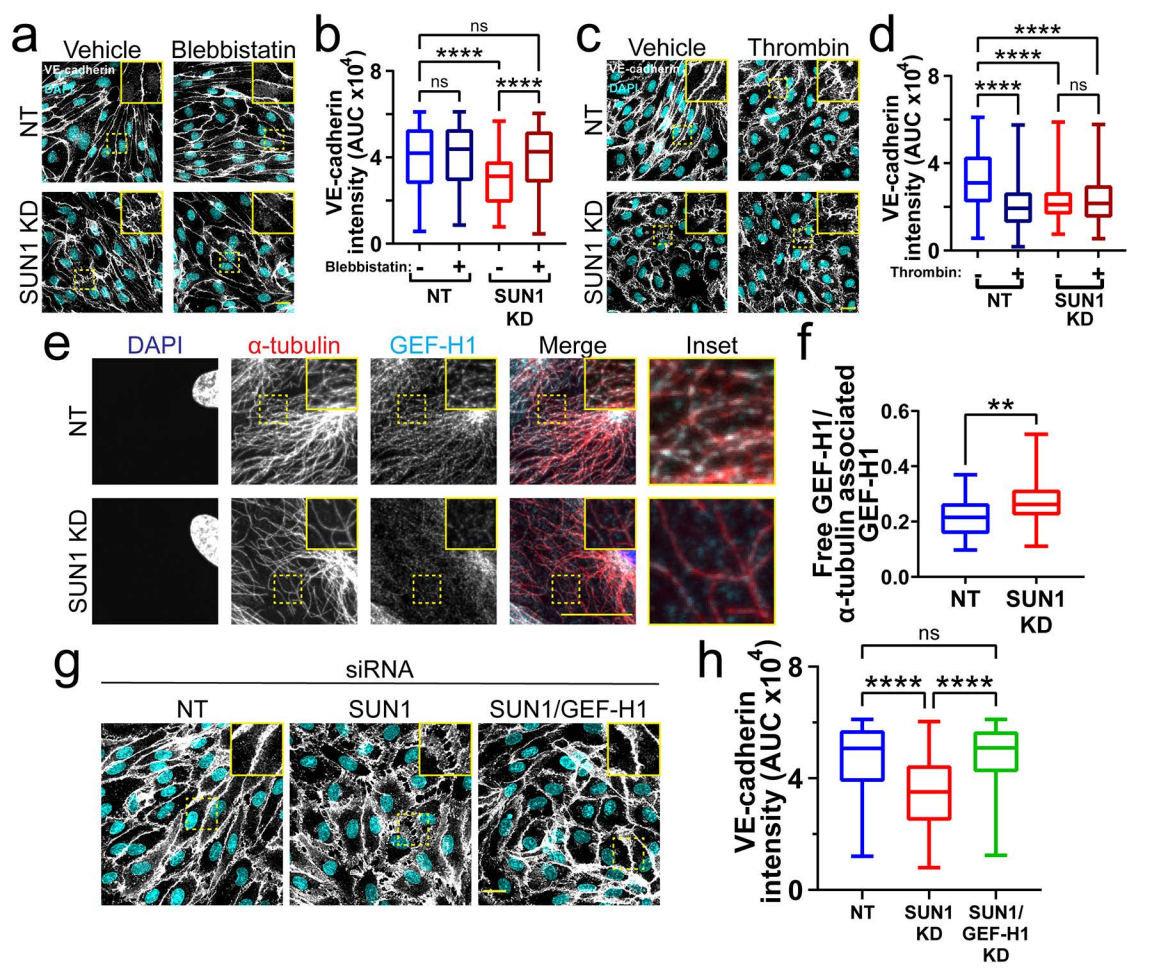
a
Vehicle
Blebbistatin
VE-cadherin
DAPI
NT
SUN1 KD
b
ns
****
ns
****
VE-cadherin intensity (AUC x10^4)
8
4
0
Blebbistatin: - + - +
NT
SUN1 KD
c
Vehicle
Thrombin
VE-cadherin
DAPI
NT
SUN1 KD
d
****
****
****
ns
VE-cadherin intensity (AUC x10^4)
8
4
0
Thrombin: - + - +
NT
SUN1 KD
e
DAPI
α-tubulin
GEF-H1
Merge
Inset
NT
SUN1 KD
f
**
Free GEF-H1/ α-tubulin associated GEF-H1
0.6
0.4
0.2
0.0
NT
SUN1 KD
g
siRNA
NT
SUN1
SUN1/GEF-H1
h
ns
****
****
VE-cadherin intensity (AUC x10^4)
8
4
0
NT
SUN1 KD
SUN1/ GEF-H1 KD

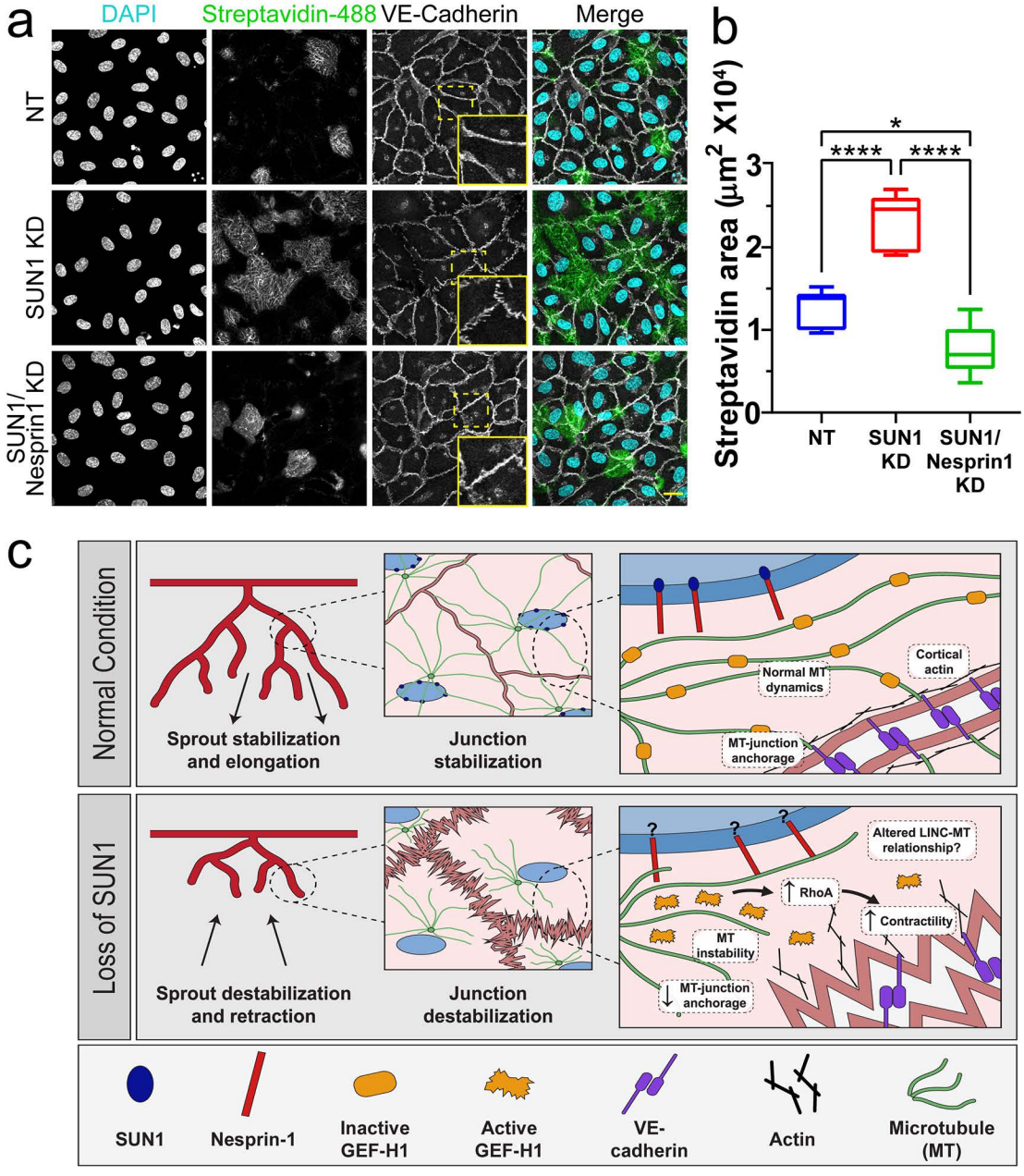
a
DAPI
Streptavidin-488
VE-Cadherin
Merge
NT
SUN1 KD
SUN1/ Nesprin1 KD
b
Streptavidin area (μm2 X10^4)
*
****
****
0
1
2
3
NT
SUN1 KD
SUN1/ Nesprin1 KD
c
Normal Condition
Sprout stabilization and elongation
Junction stabilization
Normal MT dynamics
Cortical actin
MT-junction anchorage
Loss of SUN1
Sprout destabilization and retraction
Junction destabilization
Altered LINC-MT relationship?
↑ RhoA
↑ Contractility
MT instability
↓ MT-junction anchorage
SUN1
Nesprin-1
Inactive GEF-H1
Active GEF-H1
VE-cadherin
Actin
Microtubule (MT)

Table 1. SUN1 depletion does not alter endothelial gene expression.

Condition	***# Upregulated DEG***	***# Downregulated DEG***
NT_FLOW vs NT_STAT	1323	1109
SUN1_STAT vs NT_STAT	0	1
SUN1_FLOW vs NT_FLOW	1	1

Abbr: NT, non-targeting; STAT, static; DEG, differentially expressed genes.
Red numbers indicate that single downregulated gene was *SUN1*.